A Milliarcsecond Localization Associates FRB 20190417A with a Compact Persistent Radio Source and an Extreme Magnetoionic Environment

Citation for the original published paper (version of record):
Moroianu, A., Bhandari, S., Drout, M. et al (2026). A Milliarcsecond Localization Associates FRB 20190417A with a Compact Persistent Radio Source
and an Extreme Magnetoionic Environment. Astrophysical Journal Letters, 996(1).
http://dx.doi.org/10.3847/2041-8213/ae28c7

The Astrophysical Journal Letters, 996:L16 (19pp), 2026 January 1 https://doi.org/10.3847/2041-8213/ae28c7

A Milliarcsecond Localization Associates FRB 20190417A with a Compact Persistent Radio Source and an Extreme Magnetoionic Environment

Alexandra M. Moroianu[1], Shivani Bhandari[2], Maria R. Drout[3,4], Jason W. T. Hessels[1,5,6,7], Danté M. Hewitt[1], Franz Kirsten[7,8], Benito Marcote[7,9], Ziggy Pleunis[1,7], Mark P. Snelders[1,7], Navin Sridhar[10,11], Uwe Bach[12], Emmanuel K. Bempong-Manful[13,14], Vladislavs Bezrukovs[15], Richard Blaauw[7], Justin D. Bray[13], Salvatore Buttaccio[16,17], Shami Chatterjee[18], Alessandro Corongiu[19], Roman Feiler[20], B. M. Gaensler[3,4,21], Marcin P. Gawroński[20], Marcello Giroletti[17], Adaeze L. Ibik[3,4], Ramesh Karuppusamy[12], Mattias Lazda[3,4], Calvin Leung[22,23], Michael Lindqvist[8], Kiyoshi W. Masui[24,25], Daniele Michilli[26], Kenzie Nimmo[24], Omar S. Ould-Boukattine[1,7], Ayush Pandhi[3,4], Zsolt Paragi[9], Aaron B. Pearlman[5,6], Weronika Puchalska[20], Paul Scholz[4,27], Kaitlyn Shin[28], Jurjen J. Sluman[7], Matteo Trudu[19], David Williams-Baldwin[13], and Jun Yang[8]

[1] Anton Pannekoek Institute for Astronomy, University of Amsterdam, Science Park 904, 1098 XH, Amsterdam, The Netherlands; a.m.moroianu@uva.nl
[2] SKA Observatory (SKAO), Science Operations Centre, CSIRO ARRC, Kensington WA 6151, Australia
[3] David A. Dunlap Department of Astronomy & Astrophysics, University of Toronto, 50 St. George Street, Toronto, ON M5S 3H4, Canada
[4] Dunlap Institute for Astronomy and Astrophysics, 50 St George Street, University of Toronto, ON M5S 3H4, Canada
[5] Department of Physics, McGill University, 3600 rue University, Montréal, QC H3A 2T8, Canada
[6] Trottier Space Institute, McGill University, 3550 rue University, Montréal, QC H3A 2A7, Canada
[7] ASTRON, Netherlands Institute for Radio Astronomy, Oude Hoogeveensedijk 4, 7991 PD Dwingeloo, The Netherlands
[8] Department of Space, Earth and Environment, Chalmers University of Technology, Onsala Space Observatory, 439 92, Onsala, Sweden
[9] Joint Institute for VLBI ERIC, Oude Hoogeveensedijk 4, 7991 PD Dwingeloo, The Netherlands
[10] Department of Physics, Stanford University, 382 Via Pueblo Mall, Stanford, CA 94305, USA
[11] Kavli Institute for Particle Astrophysics & Cosmology, P.O. Box 2450, Stanford University, Stanford, CA 94305, USA
[12] Max-Planck-Institut für Radioastronomie, Auf dem Hügel 69, 53121 Bonn, Germany
[13] Jodrell Bank Centre for Astrophysics, Dept. of Physics & Astronomy, University of Manchester, Manchester M13 9PL, UK
[14] School of Physics, University of Bristol, Tyndall Avenue, Bristol BS8 1TL, UK
[15] Engineering Research Institute Ventspils International Radio Astronomy Centre (ERI VIRAC) of Ventspils University of Applied Sciences, Inzenieru street 101, Ventspils, LV-3601, Latvia
[16] INAF—Osservatorio Astrofisico di Catania, via Santa Sofia 78, I-95123, Catania, Italy
[17] INAF—Istituto di Radioastronomia, Via Gobetti 101, 40129, Bologna, Italy
[18] Cornell Center for Astrophysics and Planetary Science, Cornell University, Ithaca, NY 14853, USA
[19] INAF—Osservatorio Astronomico di Cagliari, via della Scienza 5, I-09047, Selargius (CA), Italy
[20] Institute of Astronomy, Faculty of Physics, Astronomy and Informatics, Nicolaus Copernicus University, Grudziadzka 5, PL-87-100 Toruń, Poland
[21] Department of Astronomy and Astrophysics, University of California, Santa Cruz, 1156 High Street, Santa Cruz, CA 95064, USA
[22] Department of Astronomy, University of California, Berkeley, CA 94720, USA
[23] Miller Institute for Basic Research, University of California, Berkeley, CA 94720, USA
[24] MIT Kavli Institute for Astrophysics and Space Research, Massachusetts Institute of Technology, 77 Massachusetts Avenue, Cambridge, MA 02139, USA
[25] Department of Physics, Massachusetts Institute of Technology, 77 Massachusetts Avenue, Cambridge, MA 02139, USA
[26] Laboratoire d'Astrophysique de Marseille, Aix-Marseille Univ., CNRS, CNES, Marseille, France
[27] Department of Physics and Astronomy, York University, 4700 Keele Street, Toronto, ON MJ3 1P3, Canada
[28] Cahill Center for Astronomy and Astrophysics, MC 249-17, California Institute of Technology, Pasadena CA 91125, USA

Received 2025 September 5; revised 2025 November 12; accepted 2025 December 3; published 2025 December 30

Abstract

We report the milliarcsecond localization of a high ($\sim$1379 pc cm^{-3}) dispersion measure (DM) repeating fast radio burst (FRB), FRB 20190417A. Combining European VLBI Network detections of five repeat bursts, we confirm the FRB's host to be a low-metallicity, star-forming dwarf galaxy at $z = 0.12817$, similar to the hosts of FRB 20121102A, FRB 20190520B, and FRB 20240114A. We also confirm that it is associated with a previously reported persistent radio source (PRS), which is compact on milliarcsecond scales. Visibility-domain model fitting constrains the transverse physical size of the PRS to <23 pc and yields an integrated flux density of 190 ± 40 μJy at 1.4 GHz. Though we do not find significant evidence for DM evolution, FRB 20190417A exhibits a time-variable rotation measure (RM) ranging between +3958 ± 11 rad m^{-2} and +5061 ± 24 rad m^{-2} over a 50-day period. We find no evidence for intervening galaxy clusters in the FRB's line of sight and place a conservative lower limit on the rest-frame host DM contribution of 1228 pc cm^{-3} (90% confidence)—the largest known for any FRB so far. This system strengthens the emerging picture of a rare subclass of repeating FRBs with large and variable RMs, above-average host DMs, and luminous PRS counterparts in metal-poor dwarf galaxies. Our results suggest that these systems are the result of environmental selection, or a distinct engine for FRB emission.

Unified Astronomy Thesaurus concepts: Radio transient sources (2008); Transient sources (1851); Radio bursts (1339); Very long baseline interferometry (1769); High energy astrophysics (739); Burst astrophysics (187)

1. Introduction

Fast radio bursts (FRBs) are roughly millisecond-duration, highly luminous ($\gtrsim 10^{42}$ erg s^{-1}) radio transients of extragalactic origin with dispersion measures (DMs) exceeding expectations from Galactic electron density models. FRBs were discovered in 2007 (D. R. Lorimer et al. 2007), and the development of dedicated high-cadence, wide-field surveys such as CHIME/FRB (CHIME/FRB Collaboration et al. 2018; M. Amiri et al. 2021) have yielded detections of 5000+ sources so far (S. Siegel & E. Fonseca 2025). Although most FRBs appear as isolated, one-off events, $\lesssim$100 FRBs (CHIME/FRB Collaboration et al. 2023) have been observed to repeat over timescales ranging from seconds to years. The detection of an FRB-like burst from the Galactic magnetar SGR 1935+2154, coincident with an X-ray flare (C. D. Bochenek et al. 2020; CHIME/FRB Collaboration et al. 2020; S. Mereghetti et al. 2020; F. Kirsten et al. 2021; C. K. Li et al. 2021; A. Ridnaia et al. 2021; M. Tavani et al. 2021), showed that at least a fraction of FRBs are produced by magnetars. However, the observed diversity in burst morphologies, repetition rate, polarimetry, and host environments suggests that multiple source classes and/or physical processes may emit FRBs (B. Marcote et al. 2020; Z. Pleunis et al. 2021; F. Kirsten et al. 2022).

Targeted interferometric observations of active repeating sources have revealed a remarkable diversity in host and local environments. Very long baseline interferometry (VLBI) has enabled parsec-scale localization of repeaters, notably FRB 20180916B in the spiral arm of a Milky Way (MW)–like host ∼200 pc offset from a star-forming region (B. Marcote et al. 2020; S. P. Tendulkar et al. 2021) and FRB 20200120E in a globular cluster in the nearby galaxy M81 (F. Kirsten et al. 2022), suggesting a possible origin through binary merger, accretion-induced collapse, or an older compact object progenitor. Polarimetric observations place some repeaters in extreme magnetoionic environments with rapidly varying rotation measures (RMs) as high as 10^5 rad m^{-2} (D. Michilli et al. 2018), while others are found in much more quiescent environments (e.g., R. Mckinven et al. 2023; C. Ng et al. 2025).

Interestingly, a small subset of these well-localized repeaters are spatially coincident with compact, highly luminous, nonthermal persistent radio sources (PRSs) that are unresolved even at milliarcsecond resolution (see, e.g., B. Marcote et al. 2017). The compact sizes of these sources, coupled with their high radio luminosities (B. Marcote et al. 2017; C. H. Niu et al. 2022; G. Bruni et al. 2025), are inconsistent with radio emission expected from star formation. The prototypical source is FRB 20121102A, the first repeating FRB, which was found to be associated with a compact, luminous ($\sim 10^{29}$ erg s^{-1} Hz^{-1}) PRS embedded in a star-forming, low-metallicity dwarf galaxy (C. G. Bassa et al. 2017; S. Chatterjee et al. 2017; B. Marcote et al. 2017; S. P. Tendulkar et al. 2017). FRB 20121102A exhibits an extreme, evolving RM ($\sim 10^4$–10^5 rad m^{-2}; source rest frame) consistent with a highly magnetized and dynamic local environment (D. Michilli et al. 2018). A similar case is FRB 20190520B, which also shows drastic RM variability, even RM sign reversal ($[-3.6, +2.0] \times 10^4$ rad m^{-2}; source rest frame), and resides in a comparable host galaxy to FRB 20121102A (C. H. Niu et al. 2022; R. Anna-Thomas et al. 2023; S. Bhandari et al. 2023). These two systems are now considered archetypes of a subclass of FRB–PRS systems that reside in dense, magnetized local environments.

By contrast, other PRS-associated FRBs such as FRB 20201124A and FRB 20240114A have shown lower |RMs| ($\sim 10^2$ rad m^{-2}) and more modest PRS luminosities ($\sim 10^{27}$–10^{28} erg s^{-1} Hz^{-1}) and remain under active investigation as potential analogs or evolutionary counterparts to FRB 20121102A and FRB 20190520B[29] (V. Ravi et al. 2022; Y. Bhusare et al. 2024; G. Bruni et al. 2024, 2025). An empirical correlation between PRS luminosity and FRB |RM| has been proposed (Y.-P. Yang et al. 2020), suggesting that these two properties could serve as evolutionary tracers, with the youngest systems hosting the most luminous PRSs and largest |RMs|.

The physical nature of PRSs remains debated. Proposed models include magnetar wind nebulae (MWNe) inflated by relativistic particle outflows (K. Murase et al. 2016; B. D. Metzger et al. 2017; B. Margalit & B. D. Metzger 2018; B. Margalit et al. 2018), hypernebulae produced by hyper-Eddington-accreting compact objects (N. Sridhar & B. D. Metzger 2022; N. Sridhar et al. 2024), and accreting wandering massive black holes (MBHs; R. Anna-Thomas et al. 2023; Y. Dong et al. 2024a). Models invoking subenergetic supernovae that leave behind highly magnetized neutron stars in dense circumstellar environments are particularly compelling, as they can explain both the persistent emission and high Faraday rotation observed in these systems (B. D. Metzger et al. 2017; B. Margalit & B. D. Metzger 2018; A. L. Piro & B. M. Gaensler 2018).

Recently, A. L. Ibik et al. (2024) conducted a targeted search for unresolved PRSs in the roughly arcminute-level localization regions of 37 CHIME/FRB repeaters using archival surveys and targeted Karl G. Jansky Very Large Array (VLA) observations, identifying two promising candidates: PRS 20181030A-S1 and PRS 20190417A-S1. Both exhibit nonthermal spectra and remain unresolved in the VLA images (2″–5″ resolution), suggesting compact, potentially persistent emission. PRS 20190417A-S1 is in the field of FRB 20190417A, a repeating FRB with a measured DM of ∼1379 pc cm^{-3} (extragalactic component ∼1300 pc cm^{-3})—one of the highest known among repeaters (E. Fonseca et al. 2020; CHIME/FRB Collaboration et al. 2023). Its |RM| (∼4500 rad m^{-2} with $\mathrm{RM}_{\mathrm{MW}} = 36 \pm 13$ rad m^{-2}) is also large, indicating a strongly magnetized local environment consistent with those of the most luminous known FRB–PRS systems (Y. Feng et al. 2022; R. Mckinven et al. 2023).

In this Letter, we report the milliarcsecond localization of FRB 20190417A and its PRS, confirming the association proposed by A. L. Ibik et al. (2024) and demonstrating the source's compactness. We present the derived properties of the system, which appears to bridge the gap between the most luminous, high-|RM| FRB–PRS systems and those with more modest properties. We discuss the implications for PRS source models and the environments that give rise to persistent radio emission among repeating FRBs.

---

[29] We note that a compelling candidate PRS has recently been discovered within the CHIME/FRB Outrigger localization region of repeating FRB 20191106C. The repeater exhibits a high RM variability of -1044.4 ± 0.2 rad m^{-2} to -263.3 ± 0.2 rad m^{-2}, while the PRS shares similar properties to those of FRB 20121102A and FRB 20190520B, with a specific luminosity of $\sim 10^{29}$ erg s^{-1} Hz^{-1} and a nonthermal spectral index of $\alpha = -0.60 \pm 0.05$ (CHIME/FRB Collaboration et al. 2025; C. Ng et al. 2025).

2. Observations and Data Reduction

2.1. EVN Observations

We observed FRB 20190417A using the European VLBI Network (EVN) at a central frequency of 1382 MHz as part of the Pinpointing REpeating ChIme Sources with EVN dishes (PRECISE) program.[30] Twenty-five observations were conducted between 2021 October 5 and 2022 August 26 under the project codes EK050 and EK051 (PI: Kirsten). The data were correlated using the FX Software Correlator (A. Keimpema et al. 2015) at the Joint Institute for VLBI ERIC (JIVE) with an integration time of 4 s and 64 channels per 32 MHz subband. The initial pointing position for the observations was the CHIME/FRB discovery position of FRB 20190417A (E. Fonseca et al. 2020), and subsequent observations were carried out using the CHIME/FRB baseband position (D. Michilli et al. 2023). All initial correlations were performed at the centroid of the baseband localization: $\alpha(\mathrm{J2000}) = 19^{\mathrm{h}}39^{\mathrm{m}}04''$, $\delta(\mathrm{J2000}) = +59°19'\,55^{s}$, with an uncertainty of 15″ in α and 16″ in δ (D. Michilli et al. 2023).

The participating EVN stations were Effelsberg (Ef), Westerbork single dish RT1 (Wb), Toruń (Tr), Onsala (O8), Irbene (Ir), Medicina (Mc), Noto (Nt), Urumqi (Ur), and the e-MERLIN stations: Cambridge (Cm), Darnhall (Da), Defford (De), Jodrell Bank Mark II (Jb), Knockin (Kn), and Pickmere (Pi). Scheduling constraints meant that the available antennas varied between epochs. The total observing bandwidth spanned 256 MHz, divided into 8×32 MHz subbands. Not all antennas recorded the full bandwidth or were on source for entire sessions, due to differing station capabilities, local sidereal time constraints, and slewing limitations.

Each epoch consisted of alternating 5-minute scans on FRB 20190417A and 1-minute scans on the phase calibrator J1930+5948 (S-band flux density: 0.058 Jy beam^{-1}), located 1°.2 from the target. We also observed J1927+6117 (S-band flux density: 0.646 Jy beam^{-1}) as our primary fringe-finder and bandpass calibrator. A secondary calibrator, J1934+6138 (S-band flux density: 0.211 Jy beam^{-1}), located 2°.1 from the phase calibrator, served as a check source to evaluate the quality of the calibration and assess the final astrometric precision (L. Y. Petrov & Y. Y. Kovalev 2025). In total, we observed FRB 20190417A for 58.6 hr.

Raw baseband voltages recorded at Ef were processed using the PRECISE analysis pipeline[31] to search for bursts. The voltages were channelized and transformed into Stokes I (total intensity) filterbanks (D. R. Lorimer 2011) sampled at 128 μs time resolution with 31.25 kHz frequency channels using `digifil` (W. van Straten & M. Bailes 2011). The intensity data were searched with `Heimdall`[32] using a detection threshold of 7σ and DM range of 1379 ± 50 pc cm^{-3}. Burst candidates identified by `Heimdall` were then classified with `FETCH` (D. Agarwal et al. 2020), a deep learning transient classifier; we used the A and H models with a 50% probability threshold to separate likely astrophysical events from false positives. The final candidates were then inspected by eye to judge their astrophysical origin. The search pipeline is described in detail by F. Kirsten et al. (2021, 2022).

2.2. Data Calibration and Imaging

Post-correlation calibration was carried out in CASA using established VLBI procedures (J. P. McMullin et al. 2007; CASA Team et al. 2022; I. M. van Bemmel et al. 2022). FITS-IDI files for each observation were retrieved from the EVN data archive,[33] providing two separate data products: (i) continuum files, comprising visibility data for the target and each calibrator, and (ii) burst files, containing ∼millisecond time slices centered on the detected bursts. Calibration metadata were appended using the CASA VLBI extension package, `casavlbitools`,[34] including a priori amplitude calibration (station gain curves and system temperature measurements) and a priori flagging tables generated by the EVN AIPS pipeline. The FITS-IDI files were then converted into CASA Measurement Sets (MS) using the `importfitsidi` task.

Initial data inspection via `plotms` revealed artifacts from reduced antenna sensitivity in the edge channels, so the first and last four channels per subband were flagged using `flagdata`. Automated flagging was then applied using the TFCrop algorithm, with standard deviation cuts of $\sigma_{\mathrm{time}} = 4$ and $\sigma_{\mathrm{freq}} = 3$ to remove time–frequency outliers. Additional manual flagging was performed to remove persistent amplitude or phase artifacts.

Calibration proceeded in three main stages using the `fringefit` and `bandpass` tasks: (1) single-band delay calibration to correct for instrumental delays between subbands, (2) bandpass calibration to mitigate frequency-dependent gain variations, and (3) multiband delay calibration, applying global fringe fitting across the full bandwidth. For steps 1 and 2, solutions were derived using the best fringe-finder scan, with a solution determined for each spectral window. Multiband delay calibration used phase-referencing scans to correct for phase variations across the time and frequency domains.

Solutions from all stages were applied incrementally using `applycal`. The calibrated data for the phase calibrator and check sources were extracted into separate MS files using `split`. Imaging and iterative self-calibration of the phase calibrator were then performed using `tclean` and `gaincal`, producing a refined source model. This improved model allowed for enhanced phase and amplitude calibration across antennas, leading to better calibration of the check source and target.

Dirty images of the bursts and continuum field were generated in CASA using `tclean` with `niter=0` and natural weighting to prioritize sensitivity. For the burst, we produced per-baseline delay maps—signal-to-noise ratio (S/N) as a function of residual delay—and dirty images to assess the quality of each baseline. Baselines exhibiting a well-defined delay peak or a single, identifiable fringe were classified as high-S/N and retained for subsequent imaging and astrometric analysis. In contrast, noise-dominated baselines with sidelobe ambiguity (i.e., multiple fringe peaks with comparable amplitudes) were excluded to avoid introducing astrometric error and positional bias in the final burst localization.

---

[30] http://www.ira.inaf.it/precise/Home.html

[31] https://github.com/pharaofranz/frb-baseband

[32] https://sourceforge.net/projects/heimdall-astro/

[33] https://archive.jive.nl/

[34] https://github.com/jive-vlbi/casa-vlbi/

Table 1

Properties of the Bursts Detected from FRB 20190417A in This Campaign

ID	EVN Project Code	ToA[a] (MJD)	S/N[b]	Width[c] (ms)	Fluence[d] (Jy ms)	L/I (%)	C/I (%)	$\mathrm{RM_{FDF}}$ (rad m^{-2})	$\mathrm{RM_{QU}}$ (rad m^{-2})
B1	EK050C	59619.7519305064	10.3	8.2 ± 1.0[e]	0.44	60 ± 2	6 ± 2	4765 ± 27	-
B2	EK050D	59654.7669240331	11.0	0.6 ± 0.1	0.18	98 ± 9	3 ± 6	5017 ± 45	5061 ± 24
B3	EK050F	59705.5014491605	20.9	5.3 ± 0.3	1.13	83 ± 2	2 ± 1	3972 ± 16	3958 ± 11
B4	EK050G	59789.0391490897	8.3	1.6 ± 0.2	…	…	…	…	…
B5	EK050G	59789.0599048523	10.5	0.9 ± 0.1	0.15	50 ± 8	−1 ± 7	4892 ± 327	…
B6	EK051B	59796.2139888657	7.2	3.1 ± 0.5	0.25	…	…	…	…
B7	EK051A	59801.1300802646	15.8	3.9 ± 0.3	0.70	45 ± 2	5 ± 2	4907 ± 49	…
B8	EK051D	59818.1321031052	10.1	2.1 ± 0.3	0.28	81 ± 4	5 ± 4	4728 ± 37	4754 ± 13

Notes.

[a] Corrected to the solar system barycenter (TDB) to infinite frequency assuming a DM of 1379.2 pc cm^{-3}, a reference frequency of 1494 MHz, and a dispersion constant of $1/(2.41 \times 10^{-4})$ MHz^2 pc^{-1} cm^3 s at the FRB position quoted in Section 3.2.

[b] This refers to the peak S/N of the time series.

[c] Burst width is measured as the FWHM of a Gaussian fit.

[d] We estimate a conservative error of 20% on these values, which is dominated by the uncertainty on the system equivalent flux density of the Ef telescope.

[e] B1 is a multicomponent burst. The burst width was calculated to encompass both peaks.

3. Analysis and Results

3.1. Burst Properties

We detected eight bursts from FRB 20190417A over 7 of the 25 observation epochs of our PRECISE program. We used the FX Software Correlator (A. Keimpema et al. 2015) to coherently dedisperse the baseband data of the Ef telescope to 1379 pc cm^{-3} and create Stokes I files of each burst. These files have a time and frequency resolution of 0.5 ms and 125 kHz, respectively, and are written out as `sigproc` filterbank files. A plot of the temporal profiles and dynamic spectra of each burst can be found in Figure 5 (Appendix A).

The burst properties are summarized in Table 1. The bursts span an order of magnitude in width, from the narrow B2 (0.60 ± 0.1 ms) to the two-component B1 (8.2 ± 1.0 ms). Burst DMs are determined by maximizing S/N over a grid of trial DMs centered on the fiducial value of 1379 pc cm^{-3} and fitting a Gaussian to the resulting S/N–DM curve. To ensure reliability, we exclude bursts whose S/N–DM curves are broad or flat due to complex substructure and/or frequency-dependent drift.[35] This yields only two bursts (B2 and B5) with robust DM measurements: 1379.2 ± 2.4 pc cm^{-3} and 1378.6 ± 1.5 pc cm^{-3}, respectively. We find a mean DM of 1378.9 ± 1.4 pc cm^{-3} in the observer frame, consistent with contemporaneous CHIME/FRB DM measurements (∼1379 pc cm^{-3}; see A. P. Curtin et al. 2024). Placing an upper limit of $\Delta\mathrm{DM} < 2.3$ pc cm^{-3} over 3 yr, we find no significant evidence for DM evolution since discovery (E. Fonseca et al. 2020), though an increase of up to 2.3 pc cm^{-3} cannot be excluded.

We perform polarimetric calibration of the burst data from Ef (circular basis) using a test pulsar, PSR B2255+58, similar to F. Kirsten et al. 2021. Thereafter we search a range of RM values between −10,000 and +10,000 rad m^{-2} to determine at which RM trial the linearly polarized flux peaks. This is done through RM synthesis, which produces the Faraday dispersion function (FDF)—a representation of how polarized emission is distributed across Faraday depth (M. A. Brentjens & A. G. de Bruyn 2005). We report $\mathrm{RM_{FDF}}$ as the depth corresponding to the strongest peak in this distribution, with values tabulated in Table 1. Three of the bursts (B2, B3, and B8) were sufficiently bright to see the cyclical intensity fluctuations induced by Faraday rotation in Stokes Q and U across the observing band. For these bursts we also perform a QU-fit (C. R. Purcell et al. 2020) to Stokes Q/L and U/L (where $L = \sqrt{Q^2 + U^2}$ is the total linear polarization) over the spectral extent of the burst (see Appendix B). We find the RM of FRB 20190417A to be highly variable (3958 ± 11 rad m^{-2} to 5061 ± 24 rad m^{-2}; observer frame), exhibiting fractional variations of 20% and even dropping by ∼1000 rad m^{-2} over a 50-day period (Appendix B, Figure 6). These results are corroborated by recently published FAST observations, in which 47 bursts were observed from 2021 October 3 to 2022 August 13 with RMs in the range 3946.0–5225.0 rad m^{-2} (observer frame; Y. Feng et al. 2025).

3.2. Milliarcsecond Localization of FRB 20190417A

To mitigate the pointing offset between the CHIME/FRB baseband position (D. Michilli et al. 2023) and the true burst position, we adopt an iterative recorrelation scheme similar to the global fringe fitting implemented in `CASA`. For each detected burst, we compute the complex lag spectrum on a high-S/N reference baseline, polarization, and spectral window. We then derive the S/N as a function of residual group delay and fit a one-dimensional Gaussian profile to the S/N-delay curve to obtain the best-fit delay correction. Applying the derived delays to all baselines, we recorrelate the visibilities to a provisional phase center[36] ∼40″ from the baseband localization. Imaging the brightest burst (B3) reveals a well-defined “cross-fringe” pattern—the characteristic pattern expected for sparse (u, v)-coverage (see, e.g., Figure 4 of K. Nimmo et al. 2022)—with an offset of ∼57″ from the provisional phase center. Applying this offset, we recorrelate the visibilities to a final, refined phase center.[37]

Each of the eight bursts from FRB 20190417A is individually imaged, with seven bursts displaying the characteristic cross-fringe

---

[35] More precise DM estimates can be obtained by analyzing the bursts at higher time resolution and optimizing for burst substructure. This analysis is deferred to future work.

[36] $\alpha(\mathrm{J2000}) = 19^{\mathrm{h}}39^{\mathrm{m}}02^{\mathrm{s}}.16$, $\delta(\mathrm{J2000}) = +59^\circ19'24''.96$.

[37] $\alpha(\mathrm{J2000}) = 19^{\mathrm{h}}39^{\mathrm{m}}05^{\mathrm{s}}.892$, $\delta(\mathrm{J2000}) = +59^\circ19'36''.99$.

pattern. The other burst (B4; see Table 1) is strongly dominated by radio frequency interference (RFI), with no baselines yielding visible fringes, and is therefore excluded from further analysis. To assess astrometric reliability, we also image the contemporaneous check source data. For five out of seven remaining bursts, the check source positions are consistent across observation epochs, showing modest deviations (<30% of the beam FWHM) from the cataloged position. These small interepoch shifts can be incorporated into the check source positional uncertainty budget and indicate that the burst localizations for these epochs are robust. In contrast, ionospheric phase variations due to low-elevation ($\lesssim 30°$) observations caused significant check source offsets (>100% of the beam FWHM) for two observational epochs (containing B2 and B3). We omit these bursts from further analysis to avoid introducing systematic errors and ambiguity (i.e., from washing out the peak) in the final burst position.

Our final burst image is constructed by coherently combining the visibilities from the five bursts (B1, B5, B6, B7, and B8) with high S/N and stable calibration, excluding baselines with sidelobe ambiguity. A two-dimensional Gaussian fit to the combined burst visibilities yields a best-fit position for FRB 20190417A within the International Celestial Reference Frame (ICRF):

$$\alpha_{\rm FRB}(J2000) = 19^{\rm h}39^{\rm m}05\overset{\rm s}{.}8919 \ \pm 4.9 \text{ mas},$$

$$\alpha_{\rm FRB}(J2000) = +59°19'36\overset{''}{.}828 \pm 5.2 \text{ mas}.$$

The quoted positional uncertainties reflect the combined effects of (i) the formal fitting error derived from the synthesized beam shape and S/N of the detection ($\Delta\alpha = 3.60$ mas, $\Delta\delta = 3.90$ mas), (ii) uncertainties in the absolute positions of the phase calibrator (J1930+5948; ±0.19 mas) and check source (J1934+6138; ±0.13 mas), (iii) the check source positional offset ($\Delta\alpha = 3.04$ mas, $\Delta\delta = 3.09$ mas), and (iv) an estimate of the frequency-dependent shift in the phase calibrator and check source positions, conservatively ±1 mas for each. The derived position is consistent with that of the candidate PRS 20190417A-S1 reported by A. L. Ibik et al. (2024) and confirms that the host galaxy of the candidate PRS is also the host of FRB 20190417A with a PATH probability (K. Aggarwal et al. 2021) $P_{\rm PATH} = 1.0$.

3.3. Confirmation of a Compact Persistent Radio Source

We search for the candidate PRS identified by A. L. Ibik et al. (2024) within a $2'' \times 2''$ continuum field centered on FRB 20190417A. A continuum dataset is formed by integrating across the five epochs used for burst imaging, equivalent to 13.6 hr of on-source time.[38] Though we do not remove the burst windows, we find that the combined leakage from the six bursts detected during those epochs (assuming a conservative fluence of 0.3 Jy ms for the low-S/N burst B4) is 0.06 μJy; this is negligible compared to the thermal noise in an EVN continuum image ($\sim$10 μJy).

The naturally weighted dirty map of the field reveals a single point-like source (S/N $\approx$ 8) at the position

$$\alpha_{\rm PRS}\ (J2000) \ = \ 19^{\rm h}39^{\rm m}05\overset{\rm s}{.}8924 \pm 3.9 \text{ mas},$$

$$\delta_{\rm PRS}\ ({\rm J2000}) \ = +59°19'36\overset{''}{.}826 \pm 4.0 \text{ mas},$$

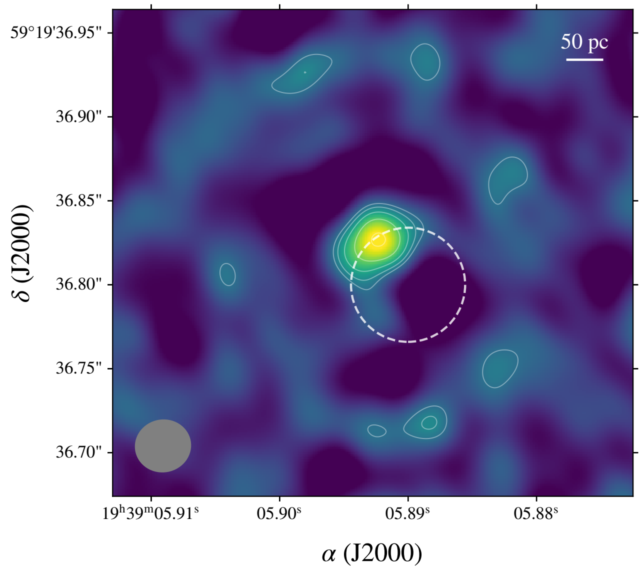

Figure 1. EVN dirty map of FRB 20190417A-PRS, as seen in the combined five epochs. A small bar in the upper right corner of the image shows a representative 50 pc transverse extent, for scale. Contour levels start at two times the rms noise level of 12 μJy beam^{-1} and increase by factors of $\sqrt{2}$. The dashed circle shows the 1σ VLA positional uncertainty of PRS 20190417A-S1 (A. L. Ibik et al. 2024). The synthesized beam is represented by the ellipse in the lower left corner; it has major and minor axes of 32.7 and 30.6 mas, respectively, and a position angle of $-10\overset{\circ}{.}8$.

referenced to the ICRF. The quoted positional uncertainties are derived using similar principles to those outlined in the previous subsection, though the uncertainty is lower owing to the better (u, v)-coverage of the continuum observations. Figure 1 shows the continuum image of the compact PRS, which we designate FRB 20190417A-PRS.

Although combining all five epochs nominally increases the integration time, the resulting visibilities are dominated by residual interepoch calibration offsets. The epoch corresponding to B4 and B5 exhibited the lowest system temperature and most stable phase solutions, yielding a check source image rms $\sim$2× better than that of the next-best epoch. We therefore use `Difmap` (M. C. Shepherd 1997) to fit a two-dimensional Gaussian to the raw visibilities of the PRS from this single epoch and place constraints on its angular size and flux density. Our best-fit model (rms $\sim$10 μJy beam^{-1}) yields a maximum angular size of <9.8 mas (1σ), corresponding to a transverse physical size of <23 pc at the redshift of the host, $z = 0.12817$. Due to the limited instantaneous bandwidth (256 MHz) and modest S/N of our observations, we are unable to measure a reliable in-band spectral index for FRB 20190417A-PRS. We therefore do not further constrain the value $\alpha = -1.2 \pm 0.4$ reported by A. L. Ibik et al. (2024). The total EVN flux density is 190 ± 40 μJy at 1.4 GHz, corresponding to a spectral luminosity of $L_{\rm 1.4GHz} = (7.4 \pm 1.5) \times 10^{28}$ erg s^{-1} Hz^{-1}. This is consistent with the flux density measurements from A. L. Ibik et al. (2024); hence, we do not find significant evidence for flux density evolution, though we note that our measurements are not tightly constrained.

The positions of the combined FRB 20190417A bursts and FRB 20190417A-PRS are consistent within their uncertainties (Figure 2, top panels). Dirty images of individual bursts obtained with sparsely sampled (u, v)-coverage can contain

---

[38] In the PRECISE program, baseband data are retained and correlated only for observations in which bursts are detected. For epochs without burst detections, the data are deleted.

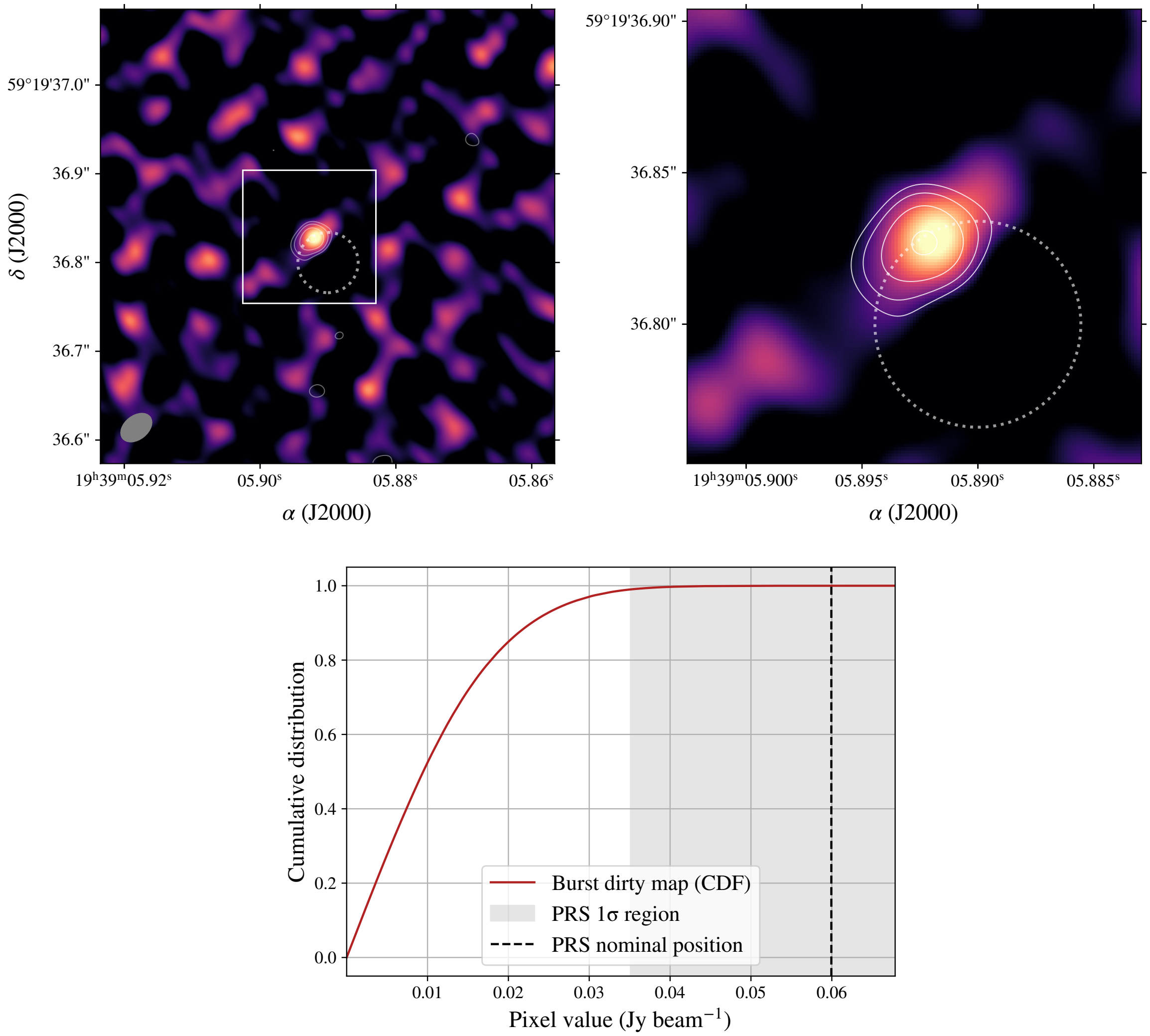

Figure 2. Top left: $0''\!.5 \times 0''\!.5$ dirty image of five combined FRB 20190417A bursts detected in our EVN-PRECISE observations. The solid contours are taken from Figure 1 and represent the EVN position of FRB 20190417A-PRS, while the dashed circle shows the 1σ VLA positional uncertainty (A. L. Ibik et al. 2024). The synthesized beam is represented by the ellipse in the lower left corner of the top left panel; it has major and minor axes of 38.8 and 26.1 mas, respectively, and a position angle of $38^{\circ}\!.5$. Top right: a zoomed-in image on the white square shown in the left panel. Bottom: CDF of the pixel values in a zoomed-out $2'' \times 2''$ field. The black dotted line shows the pixel value at the position of the EVN PRS centroid, while the gray shaded region denotes the pixel values within 1σ of the nominal PRS position.

sidelobes with amplitudes close to that of the peak intensity. These sidelobes complicate any assessment of whether another source—such as the PRS—falls on the burst source or on a sidelobe maximum. Combining multiple bursts helps remove ambiguity due to the improved (u, v)-coverage from Earth rotation. However, to quantify the spatial coincidence between the burst source and PRS, we plot a cumulative distribution function (CDF) of the pixels in a $2'' \times 2''$ dirty image of the burst and investigate how many pixels are brighter than that of the nominal PRS position (Figure 2, bottom panel). We find that only 0.0031% of pixels are brighter, ruling out a chance alignment between the two sources ($\approx 4\sigma$). Thus, our EVN localization confirms the existence of a compact radio source within the field of FRB 20190417A and constrains their angular offset to $\Delta\alpha < 8.6$ mas, $\Delta\delta < 11.0$ mas, corresponding to a maximum transverse physical offset of 20.3 pc (α) and 26.0 pc (δ) at the redshift of the host.

3.4. Host Galaxy Properties

A. L. Ibik et al. (2024) obtained deep imaging and spectroscopy of an optical source and candidate host coincident with their proposed PRS, demonstrating that it is a star-forming galaxy at $z = 0.12817$. Here we reanalyze these data to constrain additional properties of the galaxy, which we have confirmed is FRB 20190417A's host. The basic reduction of the Gemini imaging and spectroscopy is described by A. L. Ibik et al. (2024).

3.4.1. Photometry and Inferred Galaxy Mass

Images were obtained in the r, i, and z bands with the Gemini Multi-Object Spectrograph (GMOS; I. M. Hook et al. 2004). We supplement this with a g-band image obtained as part of the Dark Energy Camera Legacy Survey (DECaLS; A. Dey et al. 2019).[39] We perform aperture photometry of the host galaxy in all images using the `iraf` task `phot`. Because the host is located only $\sim 5''\!.6$ from an $m_r = 15.4$ mag star (which is saturated), the local background is complex. We determine an appropriate sky background by computing the average number of counts in an annulus around the bright star at a similar

---

[39] While the host does not have a magnitude available in the DECaLS catalog, faint emission from the source is visible in the reduced g-band image.

radius to that of the PRS host galaxy. Photometric calibration is then performed based on a set of six stars with magnitudes in the Pan-STARRS catalog (H. A. Flewelling et al. 2020). We find apparent (AB) magnitudes in all four bands of $m_g = 23.45 \pm 15$ mag, $m_r = 22.42 \pm 0.06$ mag, $m_i = 22.42 \pm 0.07$ mag, and $m_z = 23.32 \pm 0.12$ mag.[40]

We then use `Prospector`[41] (B. D. Johnson et al. 2021) to fit the revised spectral energy distribution of the host galaxy. We use the parametric (exponentially declining) star formation history model and find a best-fit stellar mass of $\log_{10}(M_*/M_\odot) = 7.88^{+0.12}_{-0.14}$. Performing synthetic photometry on the best-fit `Prospector` model, we find an absolute host rest-frame B-band magnitude of $M_B = -15.5$ Vega mag. Together, these indicate that the host is a faint dwarf galaxy.

3.4.2. Spectroscopy and Emission-line Diagnostics

The GMOS spectrum presented by A. L. Ibik et al. (2024) shows a number of strong nebular emission lines. While A. L. Ibik et al. (2024) compute a number of emission-line diagnostics, here we first perform synthetic photometry and scale the spectrum to match the observed i-band magnitude described above (to ensure accurate flux calibration; we chose i band because it contains the observed Hα feature). We then correct for MW extinction using a J. A. Cardelli et al. (1989) extinction curve and $A_V = 0.225$ mag (E. F. Schlafly & D. P. Finkbeiner 2011) and shift to host rest-frame wavelengths as discussed by A. L. Ibik et al. (2024). We measure emission-line fluxes by fitting Gaussians to the spectrum. Errors are determined via a Monte Carlo approach, creating 1000 iterations of the spectrum where each point is sampled from its respective mean and error. Final line fluxes are listed in Appendix D, Table 3.

With these revised emission-line fluxes, we confirm the results of A. L. Ibik et al. (2024) that the host galaxy falls on the star-forming sequence of the Baldwin, Phillips, and Terlevich (BPT; A. Baldwin et al. 1981) diagram. We measure an Hα flux and luminosity of $(8.15 \pm 0.02) \times 10^{-16}$ erg s^{-1} cm^{-2} and $(3.57 \pm 0.01) \times 10^{40}$ erg s^{-1}, respectively. These correspond to a star formation rate (SFR) of $0.19 \pm 0.01\, M_\odot$ yr^{-1} using the relation of E. J. Murphy et al. (2011).[42] Coupled with the galaxy stellar mass found above, this implies a specific SFR (sSFR = SFR/M_*) of $\sim 2.3 \times 10^{-8}$ yr^{-1}. Finally, we measure a gas-phase metallicity of $12 + \log(\mathrm{O/H}) = 7.95 \pm 0.01$ using the PP04 N2 diagnostic of M. Pettini & B. E. J. Pagel (2004; see Appendix D for discussion of other metallicity diagnostics). For a solar value of $12 + \log(\mathrm{O/H}) = 8.69$, this corresponds to slightly less than 20% solar.[43]

4. Discussion

The milliarcsecond localization of FRB 20190417A marks the confirmation of another FRB–PRS system and offers new insights into the growing population of PRS-associated repeating FRBs.

4.1. Characteristics of FRB 20190417A

Taking the observed DM of FRB 20190417A (1379.2 pc cm^{-3}), we decompose it into its constituent parts:

$$\mathrm{DM}_{\mathrm{obs}} = \mathrm{DM}_{\mathrm{MW}} + \langle \mathrm{DM}_{\mathrm{cosmic}}(z) \rangle + \left(\sum_i \frac{\mathrm{DM}_{\mathrm{halo},i}}{1 + z_i} \right) + \frac{\mathrm{DM}_{\mathrm{host}}}{1 + z}, \quad (1)$$

where $\mathrm{DM}_{\mathrm{MW}}$ is the Galactic contribution (including the disk and halo), $\langle \mathrm{DM}_{\mathrm{cosmic}} \rangle$ is the mean intergalactic medium (IGM) contribution, the contributions of intervening halos $\mathrm{DM}_{\mathrm{halo},i}$ are summed over, and $\mathrm{DM}_{\mathrm{host}}$ represents the contribution from the host galaxy and local environment in the source rest frame. Drawing on the methods outlined by C. H. Niu et al. (2022), J. P. Macquart et al. (2020), and S. Simha et al. (2023), we derive a distribution for $\mathrm{DM}_{\mathrm{host}}$ assuming a host galaxy redshift of $z = 0.12817$ (see Appendix C for details).

Our analysis finds a median $\mathrm{DM}_{\mathrm{host,rest}} = 1275.0$ pc cm^{-3} and places a 90% confidence lower limit $\mathrm{DM}_{\mathrm{host,rest}} > 1228.7$ pc cm^{-3}, the largest host contribution yet measured for an FRB.[44] As we do not identify any galaxy clusters in the field of FRB 20190417A (Appendix C), such an extreme $\mathrm{DM}_{\mathrm{host}}$ demands that the FRB source be embedded within, or intersect, a highly dense plasma—e.g., the ejecta of a young supernova remnant (A. L. Piro & B. M. Gaensler 2018), the regions near an active galactic nucleus (AGN; Z. Y. Zhao et al. 2024), or a compact star-forming H II region (S. K. Ocker et al. 2024; V. Prayag et al. 2024).

Although we do not find significant DM evolution with $\Delta\mathrm{DM}_{\mathrm{obs}} < 2.3$ pc cm^{-3}, FRB 20190417A's RM has varied by $\sim$20% over 6 months (Appendix B, Figure 6). Consequently, the variable RM must arise from fluctuations in the local magnetic field of the source, as our line of sight (LOS) to the FRB is not appreciably varying with time. The corresponding change in the LOS magnetic field integrated through the Faraday medium can be estimated from the RM and DM variance by

$$\Delta \langle B_\parallel \rangle = 1.23 \frac{\Delta \mathrm{RM}}{\Delta \mathrm{DM}}\ \mu\mathrm{G}. \quad (2)$$

Using $\Delta\mathrm{DM}_{\mathrm{rest}} < 2.6$ pc cm^{-3} and a net $\Delta\mathrm{RM}_{\mathrm{res}t} = 1404 \pm 33$ rad m^{-2} gives us $\Delta\langle B_\parallel \rangle > 0.65$ mG.

FAST L-band monitoring of FRB 20190417A between 2021 October and 2022 August, with a fluence completeness threshold of 0.02 Jy ms, detected 47 bursts with a peak rate of 14 h^{-1} and a mean of 2.26 h^{-1} (Y. Feng et al. 2025). Crucially, R. Mckinven et al. (2023) and Y. Feng et al. (2025) also report measurable depolarization in individual bursts from FRB 20190417A, suggesting that small-scale fluctuations in $n_e B_\parallel$ must be present. Any viable environment for FRB 20190417A must therefore sustain a strong, ordered magnetic field capable of driving large RM variations, while simultaneously allowing for the turbulence or substructure that produces the

---

[40] We note that this r-band measurement is approximately a magnitude fainter than quoted by A. L. Ibik et al. (2024). This difference can be attributed to the different means of determining the local background.

[41] https://github.com/bd-j/prospector

[42] This is essentially the same as the value from A. L. Ibik et al. (2024). Although we find lower apparent magnitudes in Section 3.4.1 above, the spectrum did not require significant scaling to match the observed photometry.

[43] While A. L. Ibik et al. (2024) list a higher (slightly supersolar) metallicity in their Appendix A.9, this was primarily due to a coding error when calculating the metallicity based on the PP04 N2 diagnostic.

[44] We note that the measured Hα flux could, in principle, be used to constrain the host DM contribution. However, our spectrum provides only a galaxy-averaged flux, introducing large uncertainties in such a conversion. We therefore defer this analysis to future work with spatially resolved Hα measurements of FRB 20190417A's local environment.

Table 2
Properties of Known FRB–PRS Systems

Property	FRB 20190417A (a)	FRB 20121102A (b)	FRB 20190520B (c)	FRB 20201124A (d)	FRB 20240114A (e)
$\mathrm{DM_{host,rest}}$ ($\mathrm{pc\ cm^{-3}}$)	>1228	$\lesssim 203$	137–707	150–220	142 ± 107
$\mathrm{RM_{rest}}$ ($\mathrm{rad\ m^{-2}}$)	5038–6441	4.4×10^{4}–1.5×10^{5}	$[-3.6, +2.0] \times 10^{4}$	-661 ± 42	449 ± 13
Peak burst rate[a] ($\mathrm{h^{-1}}$)	14	122	⋯	542	729
z	0.128	0.193	0.241	0.098	0.130
L_ν ($\mathrm{erg\ s^{-1}\ Hz^{-1}}$)	$\sim 8 \times 10^{28}$	$\sim 2 \times 10^{29}$	$\sim 3 \times 10^{29}$	$\sim 3 \times 10^{28}$	$\sim 2 \times 10^{28}$
ν of above	1.5 GHz	1.4 GHz	1.7 GHz	1.6 GHz	5 GHz
Spectral index, α	-1.20 ± 0.40	-0.15 ± 0.08	-0.41 ± 0.04	1.00 ± 0.43	-0.34 ± 0.21
Physical size (pc)	<23	$\leqslant 0.7$	<9	<700	<0.4
PRS-burst offset (pc)	<26	<40	<80	<188	~ 28
Host galaxy	Dwarf	Dwarf	Dwarf	Spiral	Dwarf

Notes.
[a] Peak rates for a fluence completeness threshold of 0.02 Jy ms.

References. (a) A. L. Ibik et al. (2024); Y. Feng et al. (2025); this work; (b) S. Chatterjee et al. (2017); S. P. Tendulkar et al. (2017); B. Marcote et al. (2017); D. Li et al. (2021); P. Wang et al. (2025); M. Bhardwaj et al. (2025a); (c) C. H. Niu et al. (2022); S. Bhandari et al. (2023); R. Anna-Thomas et al. (2023); K.-G. Lee et al. (2023); (d) G. H. Hilmarsson et al. (2021); W.-f. Fong et al. (2021); L. Piro et al. (2021); V. Ravi et al. (2022); K. Nimmo et al. (2022); Y.-K. Zhang et al. (2022); G. Bruni et al. (2024); (e) J. Tian et al. (2024); Y. Bhusare et al. (2024); J.-S. Zhang et al. (2025); G. Bruni et al. (2025); X.-L. Chen et al. (2025); M. Bhardwaj et al. (2025b).

observed depolarization through multipath propagation (see P. Beniamini et al. 2022).

4.2. Comparison with Known FRBs

Within the broader FRB population, PRS associations remain rare. While close to 100 repeating FRBs are known, fewer than 5% have been confirmed to be associated with a PRS (Y. Bhusare et al. 2024; A. L. Ibik et al. 2024). Table 2 summarizes the properties of known FRB–PRS systems. Hereafter our discussion will focus on FRB 20190417A, FRB 20121102A, FRB 20190520B, and FRB 20240114A. Their compact, nonthermal PRSs point to a likely common physical origin. By contrast, the continuum emission colocated with FRB 20201124A is not compact on milliarcsecond scales (K. Nimmo et al. 2022; V. Ravi et al. 2022) and may instead trace dust-obscured star formation in its host, making direct comparison with the four aforementioned FRB–PRS systems difficult (W.-f. Fong et al. 2021; Y. Dong et al. 2024b).

Though the sample size is small, the addition of FRB 20190417A allows us to define some emerging characteristics of these systems:

1. *Association with a PRS*: compact, nonthermal, luminous, and long-lived continuum radio sources colocated with the burst.
2. *Extreme, time-variable Faraday rotation*: LOS |RMs| ranging over 10^2–$10^5\ \mathrm{rad\ m^{-2}}$ and varying by tens of percent within months to years.
3. *Heightened burst activity*: peak burst rates exceeding the FRB median (0.5–$8\ \mathrm{h^{-1}}$ above a fluence completeness threshold of 0.02 Jy ms; Y. Feng et al. 2025), often reaching the hyperactive regime ($\sim 10^2\ \mathrm{h^{-1}}$; D. Li et al. 2021; Y. Feng et al. 2025).
4. *Large host galaxy DM contributions*: $\mathrm{DM_{host}}$ ranging over $\sim 10^2$–$10^3\ \mathrm{pc\ cm^{-3}}$.
5. *Relation to star formation in metal-poor dwarf galaxies*: predominance in low-metallicity, star-forming dwarf galaxies; FRB 20121102A and FRB 20190520B, specifically, reside near star-forming regions within their hosts (C. G. Bassa et al. 2017; C. H. Niu et al. 2022).

These properties differ from those of most FRBs, which show modest $|\mathrm{RM}| \sim 5$–$100\ \mathrm{rad\ m^{-2}}$ (A. Pandhi et al. 2024; C. Ng et al. 2025) and host DM contributions $\lesssim 100\ \mathrm{pc\ cm^{-3}}$ (I. S. Khrykin et al. 2024; L. Bernales-Cortes et al. 2025). Typical FRBs also trace the star-forming main sequence of galaxies, showing no strong metallicity preference (S. Yamasaki et al. 2025) and a bias toward massive star-forming galaxies (A. C. Gordon et al. 2023; K. Sharma et al. 2024). By contrast, the low-metallicity hosts of FRB–PRS systems (see Figure 3) mirror the galaxies that give rise to hydrogen-poor superluminous supernovae (SLSNe-I) and long gamma-ray bursts (LGRBs). This suggests a similar progenitor channel or environmental pathway linking these transients, as first explored by B. D. Metzger et al. (2017) and B. Margalit et al. (2018).

Despite the many parallels between FRB 20190417A and other PRS-associated FRBs, it occupies an intermediate position in terms of its properties—namely, its |RM| and PRS luminosity. Placing the known systems on the empirical L_ν–|RM| relation for an expanding magnetized nebula (Y.-P. Yang et al. 2020) positions FRB 20190417A as a potential bridging source connecting the most magnetized and luminous FRB–PRS systems (FRB 20121102A, FRB 20190520B) with weaker ones such as FRB 20240114A (see Figure 3 in G. Bruni et al. 2025).

4.3. Physical Interpretation

It has been proposed that FRB–PRS systems trace the youngest end of the repeating FRB population, consistent with the L_ν–|RM| relation (Y.-P. Yang et al. 2020). In this model, the large and evolving |RM| of FRB 20190417A would reflect a dynamically changing magnetoionic environment surrounding a young (10^2–10^3 yr; A. L. Piro & B. M. Gaensler 2018) central engine. However, caution is warranted when employing RM as an evolutionary tracer. The Galactic center magnetar PSR J1745−2900, for instance, exhibits a large and highly variable RM that is driven by changes in the projected magnetic field/electron column along the LOS rather than by intrinsic evolution (G. Desvignes et al. 2018). Nonetheless, the inferred LOS magnetic field for FRB 20190417A ($\Delta\langle B_\parallel\rangle > 0.65$ mG)

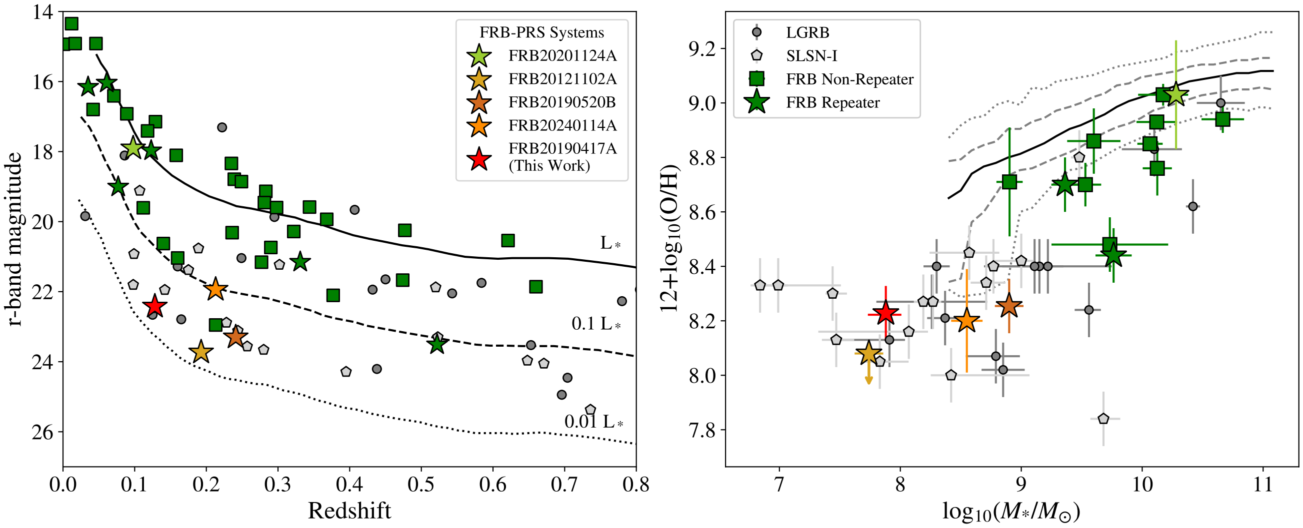

Figure 3. The host galaxy of FRB 20190417A in the context of other FRBs and energetic transients. The known FRB–PRS systems (listed in Table 2) are shown as colored stars, while other FRB hosts are shown as green stars and squares (for repeaters and nonrepeaters, respectively). Left: host galaxy apparent r-band magnitude vs. redshift. Information for FRB hosts was taken from A. C. Gordon et al. (2024) and references therein. For comparison, we also show a set of SLSN-I (pentagons) and LGRB (circles) host galaxies from R. Lunnan et al. (2014) and K. M. Svensson et al. (2010). The host galaxies of the FRB–PRS systems are notable in that, with the exception of FRB 20201124A, they are all fainter than 0.1 L_* galaxies. Right: galaxy stellar mass vs. gas-phase metallicity. Black lines represent the median, 68%, and 95% contours for Sloan Digital Sky Survey star-forming galaxies from C. A. Tremonti et al. (2004). FRB host galaxy information is taken from K. E. Heintz et al. (2020), S. Bhandari et al. (2022), and M. Bhardwaj et al. (2021); SLSN-I, from R. Lunnan et al. (2014); and LGRB, from E. M. Levesque et al. (2010). The metallicity for the SLSNe-I and LGRBs was measured using either an O3N2 diagnostic (A. S. Hirschauer et al. 2018) or an R23 diagnostic (H. A. Kobulnicky & L. J. Kewley 2004). To compare our PP04 N2 measurement from Section 3.4.2, we convert to R23 using the equations from L. J. Kewley & S. L. Ellison (2008). The host galaxies of the FRB–PRS systems are again notable: they have low masses and metallicities, more comparable to those of SLSN-I and LGRB hosts.

exceeds typical Galactic values (M. Haverkorn 2015) and is instead comparable to extreme, highly magnetized environments like those inferred near Sgr A* (R. P. Eatough et al. 2013), the PRS-associated FRB 20121102A and FRB 20190520B (D. Michilli et al. 2018; R. Anna-Thomas et al. 2023), and hyperactive repeater FRB 20240619D (O. S. Ould-Boukattine et al. 2025).

While FRB 20190417A's other properties are moderate compared to FRB 20121102A and FRB 20190520B, its exceptional DM$_{\rm host}$ complicates a straightforward evolutionary scaling. If the host contribution primarily arises from a surrounding nebula, the nebula must be significantly more dense than that of other FRB–PRS systems, pointing to a young nebula in the early stages of expansion. In such scenarios, DM evolution is expected as the nebula expands (though it can be low; A. L. Piro & B. M. Gaensler 2018). Within our EVN campaign we find no significant evolution, but we cannot exclude a slight increase (<2.3 pc cm^{-3}) similar to the early behavior of FRB 20121102A, which initially showed a modest rise in DM (D. Li et al. 2021; M. P. Snelders et al. 2025; P. Wang et al. 2025). Continued monitoring will be critical for determining whether FRB 20190417A eventually undergoes a DM decline as seen for FRB 20121102A and FRB 20190520B (C.-R. Hu & Y.-F. Huang 2023), or whether its DM remains stable.

An explanation for FRB 20190417A's extreme DM$_{\rm host}$ is that a large fraction of the excess DM does not originate from its circumsource plasma. Studies of pulsars in the MW and Magellanic Clouds show that dense H II regions and star-forming knots can add of order $\sim 10^2$ pc cm^{-3} to the DM (S. K. Ocker et al. 2024; V. Prayag et al. 2024). One extreme example, PSR J0248+6021, lies within a dense, giant H II region, which contributes an excess ~ 300 pc cm^{-3} (G. Theureau et al. 2011). By analogy, FRB 20190417A's exceptional DM$_{\rm host}$ could plausibly result from a sight line intersecting multiple dense H II regions or star-forming knots, given that these environments are natural birthplaces for young compact objects. More generally, the above-average extragalactic DMs seen in many PRS-associated FRBs (see Table 2 and Figure 4) may likewise stem from their location in, or LOS through, such star-forming knots (C. G. Bassa et al. 2017; C. H. Niu et al. 2022), potentially reflecting high gas fractions in their low-metallicity dwarf hosts.

The metal-poor environments of FRB–PRS systems also have implications for stellar evolution. Reduced line-driven winds in the late evolutionary stages of massive ($\gtrsim 8\,M_\odot$) OB stars favor the formation of massive, rapidly rotating progenitors that leave behind magnetar or BH remnants (A. Heger et al. 2003; M. P. Muno et al. 2006; A. H. Prestwich et al. 2013; D. R. Aguilera-Dena et al. 2018; C.-Y. Song & T. Liu 2023). For magnetar remnants, rapid rotation enables efficient convective and magnetorotational dynamos, producing magnetar-strength (10^{14}–10^{15} G) fields (R. Raynaud et al. 2020). The prevalence of FRB–PRS systems in these environments therefore suggests a progenitor channel linking FRBs, SLSNe-I, and LGRBs through a common end-of-life outcome: the remnant of a massive, rapidly rotating progenitor embedded in a dense, metal-poor, and highly magnetized circumstellar medium (CSM).

Taken together, these considerations motivate the question, do these systems signify (i) an evolutionary phase, (ii) an environmental selection effect, or (iii) a fundamentally distinct engine for FRB emission?

1. *Evolutionary phase.* In this picture, every repeater is born inside a luminous, magnetized nebula inflated by a newly formed compact object. As the nebula expands and fades, only the burst source remains, producing the majority

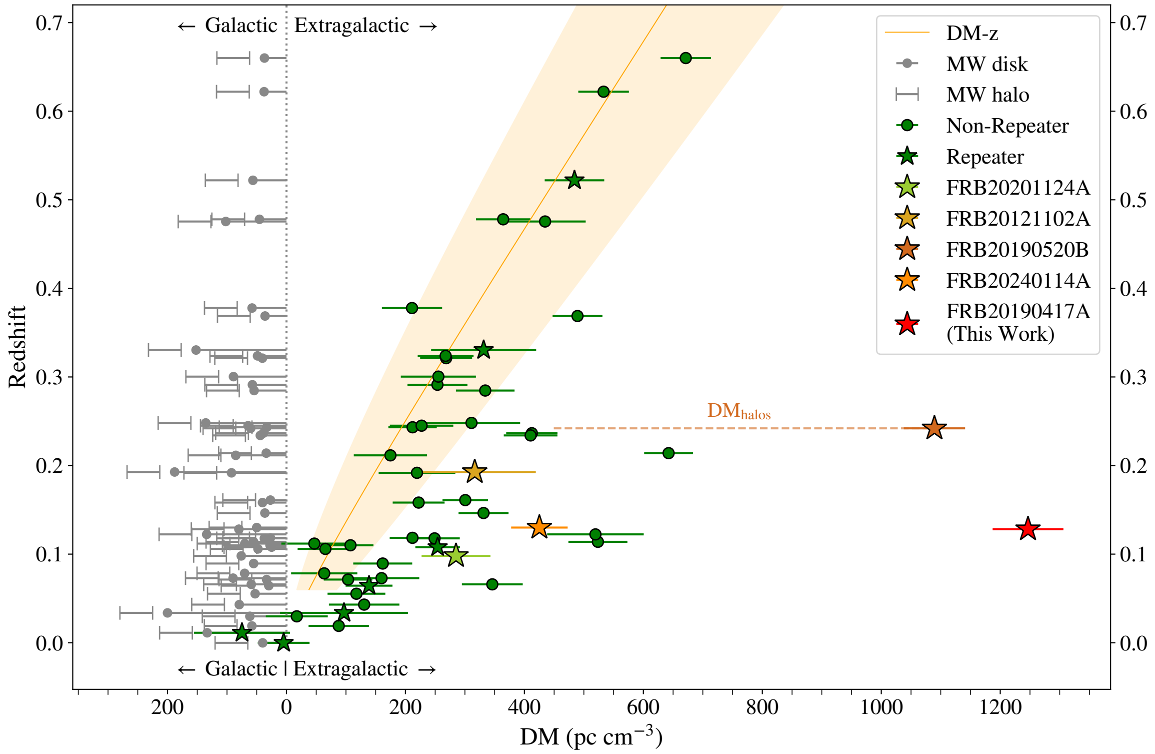

Figure 4. Figure 3 from C. H. Niu et al. (2022) updated to include 51 FRBs with robust ($P_{\rm PATH} > 0.9$) host associations and redshifts (C. J. Law et al. 2024; CHIME/FRB Collaboration et al. 2025). Galactic disk contributions are estimated from NE2001 with ±20% uncertainties, along with an additional halo contribution of 25–80 pc cm^{-3}. The red error bars on each extragalactic DM estimate represent a conservative full range uncertainty encompassing the Galactic disk and halo ranges. The expected median DM contribution of the IGM and the inner 1σ confidence interval are given by the orange line and shaded region, respectively. The known PRS-associated FRBs are shown as colored stars, while other FRBs are shown as green stars and squares (for repeaters and nonrepeaters, respectively). FRB 20190520B intersects an exceptional LOS (K.-G. Lee et al. 2023); we include its estimated DM$_{\rm halos}$ contribution for reference.

population of "PRS-quiet" repeaters, i.e., the tail end of the L_ν–|RM| relation. The rarity of bright PRSs would then reflect the brief youth of the youngest ∼5% of repeaters. This scenario is environment agnostic; luminous PRSs should be found in a variety of FRB host environments.

2. *Environmental selection.* Alternatively, FRB–PRS systems may form as a consequence of their host environment. Metal-poor, gas-rich dwarf galaxies preferentially produce rapidly rotating, massive stars (A. Schootemeijer et al. 2022). If such a progenitor leaves behind a rapidly spinning compact object (e.g., a millisecond magnetar), the loss of angular momentum over time may cause the compact object to inject its spin-down energy into the surrounding environment, creating persistent and luminous radio emission (B. D. Metzger et al. 2017; B. Margalit et al. 2018). In this case, FRB–PRS systems should remain confined to the same starburst dwarf environments that host SLSNe-I and LGRBs (Figure 3).
3. *Distinct engine.* A third possibility is that PRS-associated FRBs trace a distinct progenitor channel, rather than being by-products of youth or host environment. For example, the PRS could be powered by energetic outflows from hyper-Eddington accretion onto a compact object (N. Sridhar & B. D. Metzger 2022), while the FRB is produced along the cleaner jet funnel of the same accreting engine (N. Sridhar et al. 2021). Alternatively, the PRS could be produced by a wandering MBH, with the FRB originating from a separate compact object embedded in the same environment, or the accretion disk itself (R. Anna-Thomas et al. 2023).

At present, the properties of FRB–PRS systems—particularly, their occurrence in low-metallicity, star-forming dwarf galaxies—appear to favor either an environmental selection effect or a distinct engine origin for PRSs.

4.4. The Nature of PRSs

The discovery of PRSs has given rise to a number of theoretical models to explain their nature and association with repeating FRBs. The most prominent theories invoke MWNe, hypernebulae powered by hyper-Eddington accreting compact object binaries, and wandering MBHs.

4.4.1. Young Magnetar Wind Nebula

In this model, the FRB source is a young magnetar embedded within the expanding debris of its birth supernova. Energy injected via spin-down magnetohydrodynamic winds or episodic magnetar flares inflate a magnetized nebula inside the supernova remnant shell; synchrotron radiation from this nebula produces the observed luminous PRS (B. D. Metzger et al. 2017; B. Margalit & B. D. Metzger 2018; B. Margalit et al. 2018). The surrounding magnetoionic ejecta/CSM can yield the large, variable RMs and high DM$_{\rm host}$ typical of PRS-associated FRBs; nebular expansion and shocks also account for the evolving DMs of FRB 20121102A and FRB 20190520B (A. L. Piro & B. M. Gaensler 2018; D. Li et al. 2021; C.-R. Hu & Y.-F. Huang 2023; M. P. Snelders et al. 2025;

P. Wang et al. 2025). VLBI PRS size constraints ($\sim$0.4–23.1 pc; Table 2) are consistent with nebular expectations—for reference, the Crab Nebula, a $\sim 10^3$ yr old pulsar wind nebula (PWN), has a diameter of 3.4 pc—and the rarity of PRS-associated FRBs is compatible with the young ages ($t_{\rm age} \lesssim 10^3$ yr) implied by an MWN origin (B. Margalit & B. D. Metzger 2018; A. L. Piro & B. M. Gaensler 2018; M. Bhattacharya et al. 2024; S. M. Rahaman et al. 2025).

Another strength of the MWN model is that all confirmed FRB–PRS systems are consistent with the empirical L_ν–$|RM|$ relation predicted for evolving nebulae (Y.-P. Yang et al. 2020). Modeling efforts point to two distinct MWN regimes:

1. *Rotation powered.* M. Bhattacharya et al. (2024) show that rotation-powered MWNe with $t_{\rm age} \approx 20$ yr and initial spin periods of $P_i \approx 1$–3 ms can reproduce the properties of FRB 20121102A and FRB 20190520B and their PRSs; the same is the case for FRB 20240114A, though with $P_i \approx 10$ ms. However, S. M. Rahaman et al. (2025) argue that the internal fields required by the model ($B_{\rm int} < 10^{13}$ G) are too small to account for both the PRS and FRB emission, raising a viability issue for a purely rotationally powered origin.
2. *Magnetic decay powered.* S. M. Rahaman et al. (2025) find that compact, luminous PRSs are more naturally sustained by magnetic decay power with strong internal fields $B_{\rm int} \approx 10^{16}$–$10^{16.5}$ G, slow nebular expansion $t_d \approx 10$–300 yr, and $P_i \gtrsim 10$ ms. We note that this P_i requirement is somewhat in tension with the properties of FRB–PRS host galaxies, which favor the formation of millisecond magnetars with $P_i \lesssim 3$ ms (C.-Y. Song & T. Liu 2023). Reconciling the S. M. Rahaman et al. (2025) model with these expectations may require substantial early spin-down or a progenitor channel yielding intrinsically slower rotation.

An arising challenge for MWN models is the apparent stability of PRS emission over time, where gradual energy injection and nebular expansion should produce measurable flux evolution on decadal timescales. Long-term monitoring of FRB 20121102A-PRS shows no significant variability (A. Plavin et al. 2022; L. Rhodes et al. 2023; M. Bhardwaj et al. 2025a), though recent observations of FRB 20190520B-PRS present tentative evidence for flux decay and a low-frequency spectral break (A. Balaubramanian et al. 2025).

Targeted broadband follow-up will help discriminate between and assess the viability of MWN models for FRB–PRS systems. In particular, MWNe are expected to exhibit broadband synchrotron spectra with a low-frequency self-absorption turnover ($\sim$200 MHz) and potential high-frequency cooling breaks ($\sim$150–200 GHz) that shift toward lower frequencies as the nebula expands (S. M. Rahaman et al. 2025).

4.4.2. Accretion-powered Hypernebula

In the hypernebula scenario, N. Sridhar & B. D. Metzger (2022) propose that the PRS is powered by a compact nebula inflated by baryon-loaded outflows launched during a short-lived ($\lesssim 10^2$–10^5 yr) episode of hyper-Eddington accretion onto a compact object, just before the compact object inspirals through the donor star's envelope. In this model, forward shocks or magnetic reconnection events (at $\sim$au scales) due to flares launched along the jet funnel would power the millisecond-duration FRB (N. Sridhar et al. 2021). Particles energized at the large-scale ($\lesssim$pc) jet termination shock would emit synchrotron radiation largely in radio (PRS) and high-energy (TeV–PeV) neutrinos (N. Sridhar et al. 2024). Such powerful, turbulent outflows can naturally imprint the large host DM and variable RM observed for PRS-associated FRBs. Observations have also shown that metal-poor galaxies are more likely to host ultraluminous X-ray sources (L. Zampieri & T. P. Roberts 2009; A. H. Prestwich et al. 2013), consistent with the presence of compact objects undergoing episodes of extreme accretion. We therefore investigate the viability of this model in light of our observations of FRB 20190417A and FRB 20190417A-PRS.

Following the formalism of N. Sridhar & B. D. Metzger (2022), we estimate the observable properties of the hypernebula for an assumed set of parameters; full details are provided in Appendix E. Our calculations yield an active lifetime of the system $t_{\rm active} \sim 10^3\ {\rm yr}\ (M_\star/30\,M_\odot)(\dot{M}/10^5\,\dot{M}_{\rm Edd})^{-1}$, where $\dot{M}$ is the accretion rate and $\dot{M}_{\rm Edd} \simeq 1.4 \times 10^{19}\ {\rm g\ s^{-1}}$ is the Eddington accretion rate for an assumed $10\,M_\odot$ BH. Unlike MWN models, the radio emission is expected to plateau for a long time, or even rise/decrease slightly in the early/late stages of the nebula's evolution, depending on the system's parameters. This is consistent with the lack of significant flux evolution seen in the PRSs of FRB 20121102A and FRB 20190520B (A. Plavin et al. 2022; L. Rhodes et al. 2023; A. Balaubramanian et al. 2025; M. Bhardwaj et al. 2025a).

Powering the peak burst luminosities of FRB 20190417A (derived using FRB fluxes from E. Fonseca et al. 2020) requires an accretion rate of $\dot{M} = 10^5 \dot{M}_{\rm Edd}$. The outflowing slow winds (velocities $v_w \sim 0.01c$) from such an accretion disk would drive a forward shock into the CSM, inflating an expanding shell. The material in the expanding shell of the hypernebula contributes ${\rm DM_{host}} \approx 1100\ {\rm pc\ cm^{-3}}$ at $t_{\rm DM} = 7$ yr. At this age, the size of the expanded shell is $R_{\rm sh} = v_w t_{\rm DM} \simeq 0.02$ pc, with a smaller radio-emitting nebula confined within it; this is consistent with the upper limit on the PRS's transverse physical size of 23.1 pc. At the same age, the model also reproduces the observed PRS radio luminosity of $L_{\rm 1.4\,GHz} \approx 7.4 \times 10^{28}\ {\rm erg\ s^{-1}\ Hz^{-1}}$ (when accounting for cooling losses) for a jet speed of $v_j = 0.12c$. The maximum $|{\rm RM}|$ expected from the plasma is $|{\rm RM}|_{\rm max} \sim 10^7\ {\rm rad\ m^{-2}}$, which comfortably encompasses our observed values of $\sim$4000–5000 rad m^{-2}. In combination, these results demonstrate that the hypernebula framework can reproduce the observed properties of FRB 20190417A and its PRS under plausible assumptions. We note that this is just one of the parameter combinations that can reproduce the observables and is not a unique fit.

A challenge for the model is the brevity of its active phase ($\lesssim 10^2$–10^5 yr), which must be reconciled with the observed $\sim$5% incidence of PRSs among repeating FRBs. The short lifetime implies either that the formation rate of such binaries is relatively high or that FRB activity is preferentially triggered during the hypernebula phase. Future observations will be crucial for testing this framework and better constraining the system's parameters. Sustained flux monitoring will reveal whether FRB 20190417A-PRS plateaus, brightens, or decays, while high-frequency VLBI observations will further constrain its transverse physical size. The detection of a persistent X-ray counterpart or extended radio lobes would provide strong evidence for an accretion-powered hypernebula, though these signatures would only be detectable in exceptionally nearby systems.

4.4.3. Wandering MBH

The “wandering” (i.e., off-nuclear) MBH model posits that the PRS is powered by low Eddington accretion onto an MBH (10^4–$10^7\,M_\odot$), while the FRB arises from a separate compact object—such as a magnetar—embedded in the BH’s circumnuclear (∼0.1–10 pc) magnetoionic environment. Low Eddington accretion onto an MBH could generate a PRS via a small-scale jet or outflow, without demanding energetic youth (R. Anna-Thomas et al. 2023; Y. Dong et al. 2024a). These sources would appear as compact, quasi-steady radio emitters offset from the host galaxy center—though in dwarf galaxies the center is less well-defined.

Several observational signatures are consistent with this scenario. The large and evolving RMs and extragalactic DMs of PRS-associated FRBs are similar to those of the Galactic center magnetar PSR J1745−2900, which is embedded in the magnetoionic environment of an accreting (super)MBH (G. Desvignes et al. 2018). The low-level variability seen in FRB 20121102A-PRS over decadal timescales (A. Plavin et al. 2022; L. Rhodes et al. 2023; M. Bhardwaj et al. 2025a) is also more characteristic of a steady AGN jet than of a rapidly evolving MWN.

Targeted radio surveys have uncovered analogs of FRB PRSs in nearby dwarf galaxies. A. E. Reines et al. (2020) reported 20 off-nuclear luminous radio sources in nearby ($z < 0.055$) dwarf galaxies that are too bright to be supernova remnants or H II regions. They proposed that these sources are accreting MBHs, wandering outside the nucleus. Follow-up studies by T. Eftekhari et al. (2020) and Y. Dong et al. (2024a) found that such sources closely match FRB PRSs in radio luminosity, spectrum, and host environment. If the PRS is powered by an MBH, its radio luminosity would place it on the fundamental plane of accreting BHs, consistent with known low-luminosity AGNs (M. Mezcua et al. 2018).

A challenge for this model is its reliance on a chance coincidence between the FRB-emitting compact object and the accreting MBH. All confirmed PRS-associated FRBs exhibit above-average burst activity, and it is unclear why active sources would preferentially reside near an MBH. Moreover, deep X-ray limits for FRB 20190520B’s PRS place stringent constraints on its accretion-powered emission, implying that if it is powered by a wandering MBH, the accretion must be highly radiatively inefficient (J. Sydnor et al. 2025). At present, the wandering MBH interpretation rests largely on circumstantial evidence, bolstered by the observed long-term stability of PRS emission. High-sensitivity X-ray observations could directly probe accretion and, when combined with PRS radio luminosities, test consistency with the fundamental plane of accreting BHs. Additionally, VLBI imaging of nearby PRSs could further discriminate between a BH jet and an MWN. Finally, RM measurements of PRSs offer a complementary diagnostic: in the wandering MBH model, the |RMs| of the PRS and FRBs should be unrelated, reflecting their independent origins.

4.4.4. Other Models

Beyond the models discussed above, several alternative mechanisms have been proposed to explain the nature of PRSs. These include PWNe, off-axis afterglows from SLSNe/LGRBs, and long-lived radio emission from the interaction of supernova ejecta with the CSM.

A PWN origin is less favorable on energetic grounds. PWNe typically have radio luminosities of order $\sim 10^{34}\,\mathrm{erg\,s^{-1}}$ (B. M. Gaensler & P. O. Slane 2006), several orders of magnitude below the $\sim 10^{39}\,\mathrm{erg\,s^{-1}}$ luminosities of FRB PRSs. Off-axis SLSNe/LGRB afterglows and supernova–CSM interaction models remain viable, but they face challenges. A detailed interpretation of FRB 20190417A in the context of these models is presented in Section 6 of A. L. Ibik et al. (2024).

5. Conclusion

We have presented the milliarcsecond-precision localization of FRB 20190417A and confirmed its association with the PRS candidate identified by A. L. Ibik et al. (2024). Our key findings are as follows:

1. Combining five bursts, we localize FRB 20190417A to the position α_{FRB} (J2000) $= 19^{\mathrm{h}}39^{\mathrm{m}}05\overset{\mathrm{s}}{.}8919 \pm 4.9$ mas, δ_{FRB} ($J2000$) $= +59°19'36\overset{''}{.}828 \pm 5.2$ mas referenced to the ICRF.
2. We detect a compact, luminous radio source in the EVN continuum data of FRB 20190417A, confirming the PRS proposed by A. L. Ibik et al. (2024). We verify its spatial coincidence with FRB 20190417A and constrain their projected transverse physical offset to <26 pc. Visibility-domain model fitting constrains the angular size of the PRS to <9.8 mas, corresponding to a transverse physical size of <23 pc.
3. We demonstrate that FRB 20190417A exhibits a large, time-variable $\mathrm{RM}_{\mathrm{rest}} = 5038 \pm 14$–$6441 \pm 31\,\mathrm{rad\,m^{-2}}$, while FRB 20190417A-PRS has a luminosity of $L_{1.4\mathrm{GHz}} = (7.4 \pm 1.5) \times 10^{28}\,\mathrm{erg\,s^{-1}\,Hz^{-1}}$. The system occupies an intermediate position on the empirical L_ν–|RM| relation (Y.-P. Yang et al. 2020), between hyperactive, ultramagnetized FRB–PRS systems (FRB 20121102A, FRB 20190520B) and the fainter, lower-RM candidate FRB 20240114A.
4. Deep photometry and spectroscopy confirm that FRB 20190417A resides in a low-metallicity ($12 + \log(\mathrm{O/H}) = 7.95 \pm 0.01$) dwarf galaxy with a very high sSFR $\sim 2.3 \times 10^{-8}\,\mathrm{yr^{-1}}$, similar to the hosts of other PRS-associated FRBs. The concentration of FRB–PRS systems in the same chemically primitive, gas-rich galaxies that give rise to SLSNe and LGRBs strongly implies a metal-poor, rapidly spinning massive progenitor source.
5. Our DM decomposition analysis yields a 90% confidence lower limit $\mathrm{DM}_{\mathrm{host,rest}} > 1228.7\,\mathrm{pc\,cm^{-3}}$ and median $\mathrm{DM}_{\mathrm{host,rest}} = 1275.0\,\mathrm{pc\,cm^{-3}}$, the highest known host contribution among FRBs so far. We find that FRB–PRS systems, in general, exhibit higher-than-average $\mathrm{DM}_{\mathrm{host}}$ values and posit that this may be related to FRB–PRS systems being embedded in star-forming knots within their gas-rich hosts.
6. FRB–PRS systems are emerging as a subclass of FRBs with distinct characteristics. We discuss these commonalities in the context of three scenarios: (i) evolutionary phase, wherein all repeating FRBs pass through a bright and short-lived PRS phase shortly after birth;

(ii) environmental selection effect, wherein only FRBs born in the most metal-poor, gas-rich dwarf galaxies develop luminous PRSs; or (iii) distinct engine, wherein FRB–PRS systems might be powered by a source that is not universal to the broader FRB population. Though the evolutionary phase interpretation seems less likely, deciding among these possibilities remains an open question and will require the discovery and continued monitoring of more FRB–PRS systems.

With the addition of FRB 20190417A, the growing subclass of PRS-associated FRBs offers a unique window into the most extreme magnetoionic environments of repeating FRBs. The leading PRS models—MWNe, hypernebulae, and wandering MBHs—are each well motivated by current observations and consistent with the host environments in which FRB–PRS systems are predominantly found. Discriminating among these models will require targeted, long-term observations. In particular, we highlight the importance of (i) broadband spectral monitoring to identify turnover frequencies or cooling breaks diagnostic of nebular evolution; (ii) continued VLBI imaging of nearby PRSs to resolve structure on $\lesssim$0.1 pc scales; (iii) sustained DM, RM, and PRS flux monitoring to track temporal evolution; (iv) polarization measurements of PRS emission to determine whether the FRB and PRS share a common engine; and (v) the discovery and long-term study of new FRB–PRS systems to build a statistical sample. Such efforts will be crucial for establishing the place FRB–PRS systems hold within the broader FRB population.

Acknowledgments

The European VLBI Network is a joint facility of independent European, African, Asian, and North American radio astronomy institutes. Scientific results from data presented in this publication are derived from the following EVN project codes: EK050 and EK051. We thank the directors and staff of the participating telescopes for allowing us to observe with their facilities. This work is based in part on observations carried out using the 32 m radio telescope operated by the Institute of Astronomy of the Nicolaus Copernicus University in Toruń (Poland) and supported by a Polish Ministry of Science and Higher Education SpUB grant. S.B. is supported by a Dutch Research Council (NWO) Veni Fellowship (VI.Veni.212.058). M.R.D. acknowledges support from the NSERC through grant No. RGPIN-2019-06186, the Canada Research Chairs Program, the Canadian Institute for Advanced Research (CIFAR), and the Dunlap Institute at the University of Toronto. The AstroFlash research group at McGill University, University of Amsterdam, ASTRON, and JIVE acknowledges support from a Canada Excellence Research Chair in Transient Astrophysics (CERC-2022-00009), an Advanced Grant from the European Research Council (ERC) under the European Union's Horizon 2020 research and innovation program ("EuroFlash"; grant agreement No. 101098079), and an NWO-Vici grant ("AstroFlash"; VI.C.192.045). B.M. acknowledges financial support from the State Agency for Research of the Spanish Ministry of Science and Innovation and FEDER, UE, under grant PID2022-136828NB-C41/MICIU/AEI/10.13039/501100011033, and through the Unit of Excellence María de Maeztu 2020–2023 award to the Institute of Cosmos Sciences (CEX2019-000918-M). Z.P. is supported by an NWO Veni fellowship (VI.Veni.222.295). N.S. acknowledges support from the Simons Foundation (grant MP-SCMPS-00001470). F.K. acknowledges support from Onsala Space Observatory for the provisioning of its facilities/observational support. The Onsala Space Observatory national research infrastructure is funded through Swedish Research Council grant No. 2017-00648. C.L. acknowledges support from the Miller Institute for Basic Research at UC Berkeley. K.W.M. holds the Adam J. Burgasser Chair in Astrophysics and is supported by NSF grant 2018490. D.M. acknowledges support from the French government under the France 2030 investment plan, as part of the Initiative d'Excellence d'Aix-Marseille Université—A*MIDEX (AMX-23-CEI-088). K.N. is an MIT Kavli Fellow. A.P. is funded by the NSERC Canada Graduate Scholarships—Doctoral program. A.B.P. is a Banting Fellow, a McGill Space Institute (MSI) Fellow, and a Fonds de Recherche du Quebec—Nature et Technologies (FRQNT) postdoctoral fellow. P.S. acknowledges the support of an NSERC Discovery grant (RGPIN-2024-06266).

Data Availability

Uncalibrated visibilities of FRB 20190417A (both the bursts and the associated PRS) and its calibration sources can be downloaded from the JIVE/EVN archive, https://archive.jive.eu, under project codes EK050C, EK050D, EK050F, EK050G, EK051A, EK051B, and EK051D. Filterbank files, calibrated burst visibilities, dirty maps fits files, and the scripts that made Figures 1, 2, 4, and 6 can be accessed in our Zenodo reproduction package: doi:10.5281/zenodo.17582142. Due to the large file sizes, the burst baseband data (i.e., raw voltages) and calibrated continuum visibilities will be made available by the authors upon reasonable request.

Facility: EVN.

Software: FX Software Correlator (A. Keimpema et al. 2015), CASA (J. P. McMullin et al. 2007; CASA Team et al. 2022; I. M. van Bemmel et al. 2022), Difmap (M. C. Shepherd 1997), Astropy (Astropy Collaboration et al. 2013), Sigproc (D. R. Lorimer 2011).

Appendix A
Burst Dynamic Spectra

Figure 5 shows all temporal profiles and dynamic spectra of the bursts detected by the Ef telescope in this campaign.

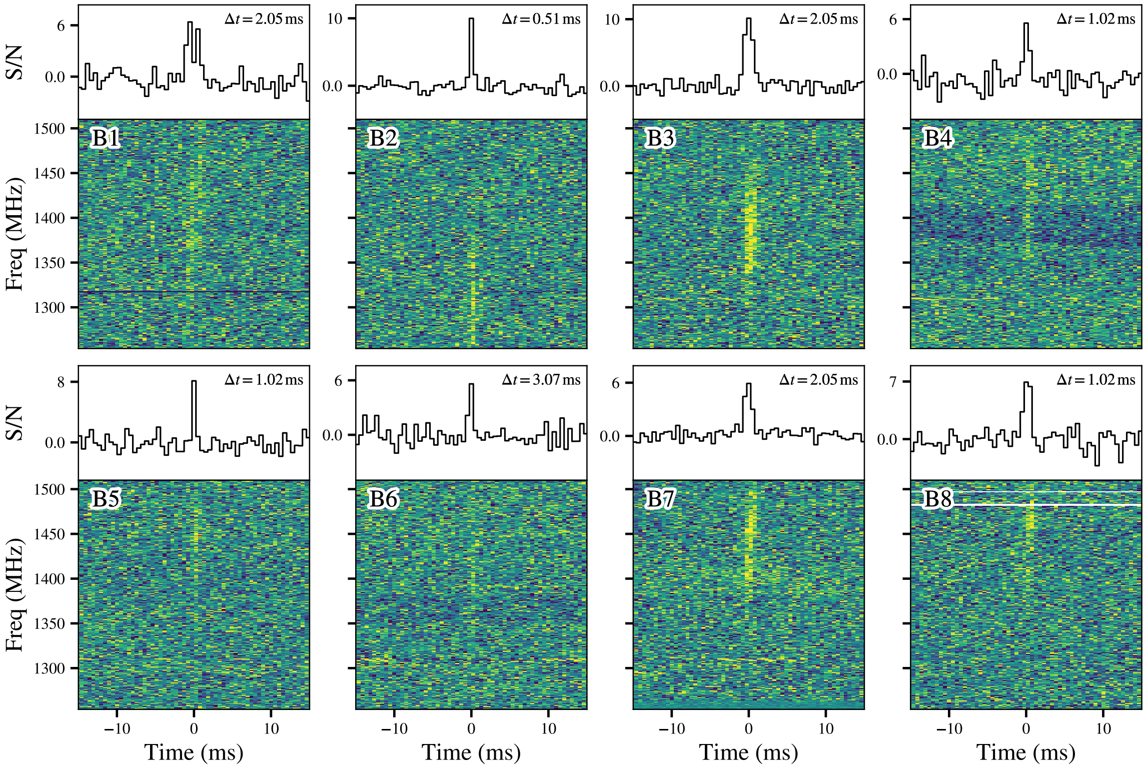

Figure 5. Temporal profiles (top) and dynamic spectra (bottom) of the eight FRB 20190417A bursts detected with the Ef radio telescope. Each burst is coherently dedispersed to a DM of 1379.0 pc cm^{-3} and is shown with a frequency resolution of 1 MHz; the time resolutions are shown in the upper right corners of each panel. Horizontal white bands correspond to frequency channels that have been flagged owing to RFI. The limits of the color map have been set to the 20th and 98th percentiles of each dynamic spectrum. We note that some of the wider bursts appear slightly over-dedispersed; future work will analyze all bursts at a higher time resolution to place tighter constraints on their DM.

Appendix B
Polarimetry

We perform polarimetric calibration of the burst data from Ef (circular basis) using a test pulsar instead of a noise diode (similar to, e.g., F. Kirsten et al. 2021). During each of our EVN observations, one/two scans of a few minutes were conducted on the pulsar B2255+58. For each pulsar scan, we measure the instrumental delay between the polarization hands by first derotating the Q and U data using the known RM of the pulsar ($-323.5\,\mathrm{rad\,m^{-2}}$) and then searching for the delay (in the range of -20 to $+20$ ns), which maximizes the linear polarized flux. For each trial the linear polarization vector ($Q + iU$) of the pulsar data is thus multiplied by a phase correction:

$$\phi_{\mathrm{corr}} = \exp(-2i(c^2\,\mathrm{RM}/\,\nu^2 + \pi\nu\tau)), \tag{B1}$$

where $\mathrm{RM} = -323.5\,\mathrm{rad\,m^{-2}}$ (R. N. Manchester et al. 2005),[45] c is the speed of light, ν is the observing frequency, and τ is the cable/instrumental delay between the polarization hands. The delays measured using this method range from ∼1 to 4 ns and vary by a few percent between pulsar observations conducted on the same day (∼10 hr apart). In order to replicate the polarimetric profile of PSR B2255+58 in the EPN database (D. M. Gould & A. G. Lyne 1998), we assume a flip between the polarization hands (equivalent to changing convention).

We then derotate the linear popularization vector of each burst from FRB 20190417A by multiplying by a phase correction using the measured delay from the pulsar. Thereafter, we search a range of RM values between $-10{,}000$ and $+10{,}000\,\mathrm{rad\,m^{-2}}$ to determine at which RM trial the linear polarized flux peaks. This is done through RM synthesis, which produces the FDF—a representation of how polarized emission is distributed across Faraday depth (M. A. Brentjens & A. G. de Bruyn 2005). We report $\mathrm{RM_{FDF}}$ as the depth corresponding to the strongest peak in this distribution, with values tabulated in Table 1. In our analysis, we assume that the sources are Faraday simple (i.e., described by a single Faraday component). We note that this assumption may lead to a slight underestimation of the RM uncertainties in the presence of Faraday complexity. However, all FDF detections in our burst sample exceed $\mathrm{S/N} = 6$, with B5 being the faintest at $\mathrm{S/N} = 5.8$.

Three of the bursts (B2, B3, and B8) were sufficiently bright to see the cyclical intensity fluctuations induced by Faraday rotation in Q and U across the observing band. For these bursts, we also perform a QU-fit (C. R. Purcell et al. 2020) to Stokes Q/L and U/L (where $L = \sqrt{Q^2 + U^2}$ is the total linear polarization) over the spectral extent of the burst. We use the following equations:

$$Q/L = \cos(2(c^2\mathrm{RM}/\nu^2 + \nu\pi\tau + \phi)) \tag{B2}$$

$$U/L = \sin(2(c^2\mathrm{RM}/\nu^2 + \nu\pi\tau + \phi)), \tag{B3}$$

with ϕ referring to an additional phase term related to the polarization position angle at infinite frequency. The delay is fixed to the delay that maximized the linear polarized flux of

---

[45] https://www.atnf.csiro.au/research/pulsar/psrcat/

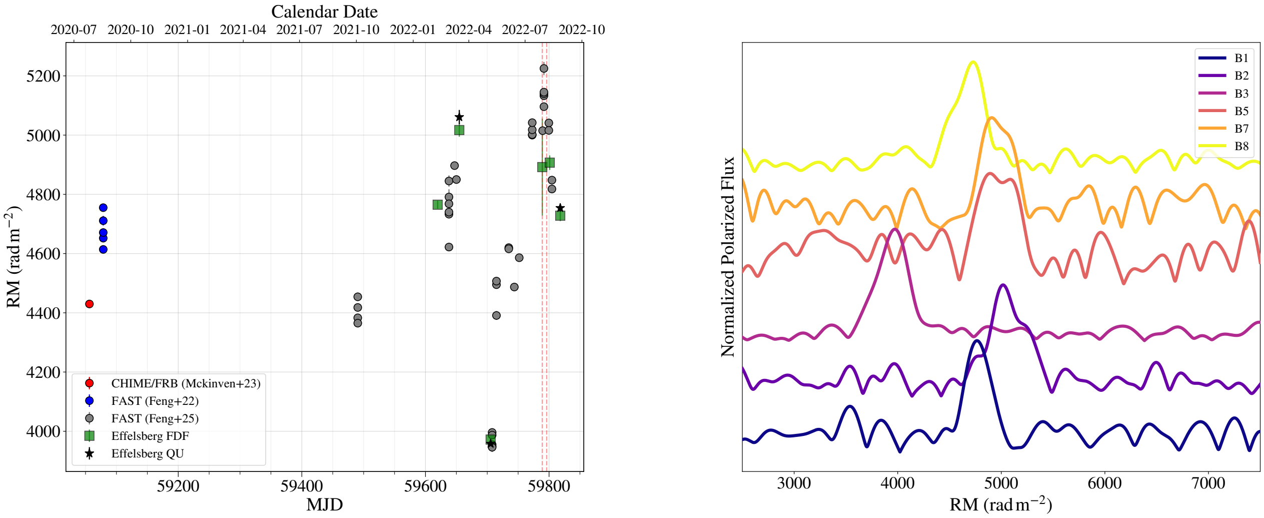

Figure 6. Left: the RM evolution of FRB 20190417A. Previous RM measurements are taken from Y. Feng et al. (2022; blue circles), R. Mckinven et al. (2023; red circle) and Y. Feng et al. (2025; gray circles). The green squares indicate RM measurements obtained using a brute-force search to maximize linear polarization. The error bars are calculated as FWHM/(S/N) of the brightest peak in the FDF. The black stars indicate the RM measurements obtained from a *QU*-fit for the bursts that were sufficiently bright. Vertical dashed lines indicate the MJDs of B4 and B6 that had too low S/N to obtain an RM measurement. Right: FDFs of the FRB 20190417A bursts detected with Ef. The instrumental delay has already been accounted for, so the shift in the peak indicates significant variation in the RM of the source.

the pulsar observation. These RM measurements (RM_{QU} in Table 1) are consistent with those obtained by maximizing linear polarization. All RM measurements can be visualized in Figure 6.

Appendix C
DM Decomposition Method

Here we adopt a deliberately conservative approach designed to avoid overestimating the $\mathrm{DM_{host}}$ contribution of FRB 20190417A. The rest-frame host contribution of an FRB can be obtained by rearranging Equation (1) as follows:

$$\mathrm{DM_{host,rest}} = (1+z)\left(\mathrm{DM_{obs}} - \mathrm{DM_{MW}} - \langle \mathrm{DM_{cosmic}}(z)\rangle - \sum_i \frac{\mathrm{DM}_{\mathrm{halo},i}}{1+z_i}\right), \qquad \text{(C1)}$$

where $\mathrm{DM_{MW}}$ is the Galactic contribution (including the disk and halo), $\langle \mathrm{DM_{cosmic}}\rangle$ is the mean IGM component, and $\mathrm{DM}_{\mathrm{halo},i}$ denotes the contribution from intervening halos along the LOS.

The MW disk contribution is estimated using the NE2001 electron density model (J. M. Cordes & T. J. W. Lazio 2002; S. K. Ocker & J. M. Cordes 2024). For the FRB's Galactic coordinates $(l,\ b) = (92^\circ\!.21,\ +19^\circ\!.50)$, the model returns $\mathrm{DM_{MW,disk}} = 78.0\ \mathrm{pc\ cm^{-3}}$. We adopt a uniform prior centered on this value $\mathrm{DM_{MW,disk}} \sim \mathcal{U}(78.0 \pm 0.2\ \mathrm{DM_{MW,disk}})\ \mathrm{pc\ cm^{-3}}$, corresponding to a ±20% uncertainty on the NE2001 estimate. The MW halo component is less certain; based on constraints on the circumgalactic medium (A. M. Cook et al. 2023; V. Ravi et al. 2025), we assume a conservative $\mathrm{DM_{MW,halo}} \sim \mathcal{U}(10,\ 111)\ \mathrm{pc\ cm^{-3}}$. Combining these components, we obtain a total MW contribution of $\mathrm{DM_{MW}} = \mathrm{DM_{MW,disk}} + \mathrm{DM_{MW,halo}}$.

Following the formalism of J. P. Macquart et al. (2020), the mean IGM contribution is

$$\langle \mathrm{DM_{cosmic}}(z)\rangle = \frac{3cH_0\Omega_b f_{\mathrm{IGM}}}{8\pi G m_p}\int_0^z \frac{(1+z')f_e(z')}{E(z')}\,dz', \qquad \text{(C2)}$$

where $H_0 = 67.4\ \mathrm{km\ s^{-1}\ Mpc^{-1}}$, $\Omega_b = 0.049$, $f_{\mathrm{IGM}} = 0.85$, and $f_e(z') \approx 7/8$ is the free electron number per baryon in the Universe (Planck Collaboration et al. 2020). At the redshift of the host, $z = 0.12817$, we find $\langle \mathrm{DM_{cosmic}}\rangle \approx 110\mathrm{pc\ cm^{-3}}$. By explicitly including a $\mathrm{DM_{halos}}$ term, we effectively account for fluctuations from intervening overdensities in the IGM and thus assume that the residual scatter in $\langle \mathrm{DM_{cosmic}}(z)\rangle$ is negligible compared to the variance introduced by halos.

FRB 20190520B has demonstrated that exceptional LOS scenarios, such as an FRB passing through multiple galaxy clusters, can inflate its DM (K.-G. Lee et al. 2023). In the case of FRB 20190417A, we cross-match the burst position with the optically selected cluster catalog of Z. L. Wen & J. L. Han (2024). We rule out FRB 20190417A intersecting a cluster or group of mass $\gtrsim 5 \times 10^{13}\ M_\odot$ within $2.8 \times r_{500}$, where r_{500} corresponds to the radius, r, within which the mean density is 500 times the critical density (Z. L. Wen & J. L. Han 2024).

To account for additional intervening halos, we draw from the methods outlined in J. X. Prochaska & Y. Zheng (2019), T. McClintock et al. (2019), and S. Simha et al. (2023). Since we ruled out intersecting halos $\gtrsim 5 \times 10^{13}\ M_\odot$, we adopt three mass bins for our $\mathrm{DM_{halo}}$ analysis—dwarf galaxies $(10^8–10^{11}\ M_\odot)$, L^* galaxies $(10^{11}–10^{13}\ M_\odot)$ and galaxy groups $((1–5) \times 10^{13}\ M_\odot)$. Each halo is assigned a hot-gas fraction, f_{hot}: $0.02 f_b$ for dwarfs, $0.15 f_b$ for L^* galaxies, and $0.3 f_b$ for groups, where $f_b = \Omega_b/\Omega_m \approx 0.158$ is the cosmological baryon fraction (Planck Collaboration et al. 2020).

Halo concentrations, c, are calculated with the `Colossus` concentration module (B. Diemer 2018) using the B. Diemer & M. Joyce (2019) mass–concentration relation, while virial radii r_{200} are obtained by inverting the spherical overdensity definition:

$$r_{200} = \left(\frac{3M_{200}}{4\pi\ 200\rho_{\mathrm{crit}}(z)}\right)^{1/3}, \qquad \text{(C3)}$$

where ρ_{crit} is the critical density ($\mathrm{kg\ m^{-3}}$). Assuming that the hot-gas component traces a dark matter Navarro–Frenk–White

(NFW) profile (J. F. Navarro et al. 1996), the electron density is

$$n_e(r) = \frac{n_0}{x(1+x)^2}, \tag{C4}$$

with $x = r/r_s$, where $r_s = r_{200}/c$ is the scale radius of the NFW profile. The central normalization, n_0, is solved analytically so that the integral of n_e out to r_{200} equals the allocated hot-gas mass. For a sight line intersecting a halo at impact parameter $b < r_{200}$, our analysis carries out a 1D line integral along the chord length $l_{\rm max} = \sqrt{r_{200}^2 - b^2}$. The resulting column density is converted to DM units and divided by $(1 + z)$ to place it in the observer frame for consistency with the rest of the analysis.

We populate the LOS with intervening halos using the J. Tinker et al. (2008) halo mass function as implemented in `Colossus`. Masses are drawn via inverse-transform sampling of the pretabulated cumulative function; z is sampled uniformly in comoving distance to preserve the expected comoving number density, $n_c(M, z)$. Using the formalism of J. X. Prochaska & Y. Zheng (2019), we compute the expected number of intercepts for each mass bin as

$$\langle N \rangle = \int_0^z n_c(M, z)\sigma(M)\frac{dX}{dz}\, dz, \tag{C5}$$

where $\sigma(M) = \pi R^2$ is the cross-sectional area of the halo (Mpc^2) and $\frac{dX}{dz} = (1+z)^2/E(z)$, with $E(z)$ referring to the dimensionless Hubble parameter (D. W. Hogg 1999). For simplicity, we assume a representative halo mass and radii per mass bin—$M_{200} \sim 10^9\, M_\odot$, $R_{200} = 60$ kpc for dwarf galaxies; $M_{200} \sim 10^{12}\, M_\odot$, $R_{200} = 250$ kpc for L* galaxies; $M_{200} \sim 3 \times 10^{13}\, M_\odot$, $R_{200} = 500$ kpc for groups (S. Giodini et al. 2009; A. V. Kravtsov 2013; T. M. Callingham et al. 2019). This results in $\langle N_{\rm dwarf} \rangle = 4.14$, $\langle N_{{\rm L}*} \rangle = 0.13$, and $\langle N_{\rm group} \rangle = 0.02$ at $z = 0.12817$. Assuming that the number of intervening halos per mass bin follows a Poissonian distribution with $\lambda = \langle N \rangle$, we simulate the expected DM per mass bin for 1,000,000 Monte Carlo sight lines. We then sum the contributions, returning both the total DM$_{\rm halos}$ and its breakdown by mass bin.

Finally, we combine the distributions of DM$_{\rm MW}$, $\langle$DM$_{\rm cosmic}\rangle$, and DM$_{\rm halos}$ to compute the posterior on DM$_{\rm host}$. Note that, by adding an explicit DM$_{\rm halos}$ term on top of $\langle$DM$_{\rm cosmic}\rangle$, we are partially double-counting the intervening halo contribution. We retain this term to be conservative; our 90% confidence lower limit on DM$_{\rm host}$ is insensitive to the tail of the distribution, and adopting tighter constraints would only raise the inferred lower limit.

Our analysis finds a median DM$_{\rm host,obs}$ = 1130.0 pc cm^{-3} and places a 90% confidence lower limit on DM$_{\rm host,obs}$ > 1088.8 pc cm^{-3} in the observer's frame, the largest known host contribution among repeaters. In the source rest frame, this corresponds to a median of DM$_{\rm host,rest}$ = 1275.0 pc cm^{-3} and a 90% confidence lower limit on DM$_{\rm host,rest}$ > 1228.7 pc cm^{-3}, indicating that FRB 20190417A resides in an exceptionally dense environment.

Appendix D
Additional Host Galaxy Information

D.1. Emission-line Fluxes

In Table 3 we list the emission-line fluxes found for the host galaxy based on the analysis described in Section 3.4.2. However, we note that the Hβ and [O III] line fluxes should be treated with caution. As noted in A. L. Ibik et al. (2024), the spectrum shows a very low (possibly unphysical) Balmer decrement of Hα/Hβ = 0.94. This is in stark contrast to the typical value of 2.87 for case B recombination at 10,000 K (D. E. Osterbrock & G. J. Ferland 2006) or even larger values expected when additional reddening is present. While it is possible to achieve Balmer decrements near unity if the emitting material has very high densities ($n_e \gtrsim 10^{13}$ cm^{-3}; S. A. Drake & R. K. Ulrich 1980; E. M. Levesque et al. 2014), this could also indicate an issue with the original flux calibration of the spectrum.

In particular, at the redshift of the host galaxy, both Hβ and the [O III] lines are close to the edge of where the sensitivity of the GMOS R400 grating falls off in the blue. Flux calibration uncertainties can therefore increase in this region (we note that the uncertainties quoted in Table 3 are purely statistical). While photometry of the host galaxy can be used to correct the flux calibration (including a possible warping with wavelength), the Hβ and the [O III] lines lie just blueward of the observed r band and we do not have complete spectral coverage for the g band. We therefore opted to perform a single vertical offset for the final spectrum based on the observed i-band magnitude for the galaxy, as described in Section 3.4.2. It is for this reason that we opt to use the PP04 N2 diagnostic (which relies only on emission lines located within the observed i band) as opposed to other diagnostics (such as the recent O3N2 calibration of A. S. Hirschauer et al. 2018, which has been used in other recent FRB studies but relies on all of the Hα, [H II], Hβ, and [O III] lines).

Finally, we note that even if the Hβ and the [O III] line fluxes are overestimated, we do not expect our conclusion that the host overlaps with star-forming galaxies (as opposed to AGNs) in the BPT diagram to change. Unlike several metallicity diagnostics, the BPT diagram relies solely on the ratios of lines located at similar wavelengths (O IIIλ5007/Hβ and [N II] λ6583/Hα), which helps to mitigate uncertainties with either flux calibration or reddening. In particular, because the ratio of [N II] λ6583 to Hα is so large (log([N II]/Hα) = −1.66), we would require log([O III]/Hβ) $\gtrsim$ 1

Table 3
Measured Emission-line Fluxes for the Host Galaxy

Emission Line	Flux (erg s^{-1} cm^{-2})
Hα λ6563	$(8.15 \pm 0.02) \times 10^{-16}$
Hβ λ4861	$(8.69 \pm 0.02) \times 10^{-16}$
[N II] λ6583	$(1.78 \pm 0.01) \times 10^{-17}$
[S II] λ6716	$(3.88 \pm 0.01) \times 10^{-17}$
[S II] λ6731	$(3.77 \pm 0.01) \times 10^{-17}$
[O III] λ4959	$(9.20 \pm 0.02) \times 10^{-16}$
[O III] λ5007	$(1.75 \pm 0.01) \times 10^{-15}$

Note. Hβ and [O III] lines fluxes may be overestimated owing to a flux calibration issue in the blue portion of the spectrum (see text for details).

in order for the galaxy to fall in the AGN portion of the BPT diagram. This, in turn, would require the relative flux calibration between λ5007 and λ4861 to be off by more than a factor of 6 (whereas resolving the Balmer decrement discrepancy would only require the relative flux calibration between Hα and Hβ—a much larger wavelength range—to be off by a factor of 2–3).

Appendix E
FRB 20190417A in the Context of the Hypernebula Model

We investigate the viability of the accretion-powered hypernebula model in light of our FRB 20190417A observations. Note that this is just one of the parameter combinations of the hypernebula system that can reproduce the observables and is not a unique fit.

Following the equations presented in N. Sridhar & B. D. Metzger (2022), we estimate the observable properties of the hypernebula assuming the following physical parameters: the jet magnetization (ratio of magnetic to plasma enthalpy density) $\sigma_j = 0.1$, the disk-wind-to-jet-luminosity ratio $\eta = 0.1$, the fraction of the shock power that goes into heating the electrons $\epsilon_e = 0.5$, and the mass of the companion accretor star $M_\star = 30\,M_\odot$. This sets the active lifetime of the system to be $t_{\rm active} \sim 10^3\,{\rm yr}\,(M_\star/30\,M_\odot)(\dot{M}/10^5\,\dot{M}_{\rm Edd})^{-1}$, where $\dot{M}$ is the accretion rate and $\dot{M}_{\rm Edd} \simeq 1.4\times10^{19}\,{\rm g\,s^{-1}}$ is the Eddington accretion rate for an assumed BH of mass $M_\bullet = 10\,M_\odot$.

Let us consider the peak radio burst luminosity from FRB 20190417A to be 10^{41}–$10^{42}\,{\rm erg\,s^{-1}}$, adopting FRB fluxes from E. Fonseca et al. (2020) and the host redshift of $z = 0.12817$. Powering this would require an accretion rate of $\dot{M} = 10^5\dot{M}_{\rm Edd}$. The outflowing slower winds (with a speed $v_w \sim 0.01c$) from such an accretion disk would drive a forward shock into the CSM with an assumed density $n \approx 10\,{\rm cm^{-3}}$. They would freely expand until a time

$$t_{\rm free} = 424\ {\rm yr}\left(\frac{L_{w,\,41}}{n_1}\right)^{1/2}\left(\frac{v_w}{0.01c}\right)^{-2/5}, \tag{E1}$$

where $L_w = \dot{M}v_w^2/2 = 6\times10^{40}\,{\rm erg\,s^{-1}}$ is the power of the outflowing winds. Here we adopt the shorthand notation $Y_x \equiv Y/10^x$ for quantities in cgs units. The contribution of the expanding material to the DM (assuming that the material remains ionized), during the free expansion phase, is given by

$$\begin{aligned}{\rm DM}_{\rm sh} &\simeq \frac{M_{\rm sh}}{4\pi R^2 m_p}\\ &\approx \begin{cases} 18\ {\rm pc\ cm^{-3}}\left(\dfrac{\dot{M}}{10^5\dot{M}_{\rm Edd}}\right)\left(\dfrac{v_w}{0.01c}\right)^{-2}\left(\dfrac{t}{424\ {\rm yr}}\right)^{-1} & (t < t_{\rm free})\\ 10\ {\rm pc\ cm^{-3}}\left(\dfrac{L_{w,\,41}}{n_1}\right)^{1/5}\left(\dfrac{t}{424\ {\rm yr}}\right)^{3/5} & (t > t_{\rm free}),\end{cases}\end{aligned} \tag{E2}$$

where we take the mass in the expanding shell to be $M_{\rm sh} \sim \dot{M}t$, and $m_p = 1.67\times10^{-24}$ g is the proton's mass. We see that at a time $t_{\rm DM} = 7$ yr the material in the expanding shell contributes a DM of ${\rm DM}_{\rm host} \approx 1100\,{\rm pc\,cm^{-3}}$, as seen from FRB 20190417A. The other solution of $t = 10^6$ yr (for $t > t_{\rm free}$) is beyond the lifetime of the system, so we do not consider it. At this age, the size of the expanded shell is $R_{\rm sh} = v_w t_{\rm DM} \simeq 0.02$ pc, with a smaller radio-emitting nebula confined within it; this is consistent with the upper limit on the PRS's transverse size of 23.1 pc. This model, at $t = t_{\rm DM}$, consistently also reproduces the observed PRS spectral luminosity of $L_\nu = 7.4\times10^{28}\,{\rm erg\,s^{-1}\,Hz^{-1}}$ (at 1.4 GHz)—taking into account the effects of various cooling losses—for a faster jet speed of $v_j = 0.12c$ (see Equations (29)–(42) of N. Sridhar & B. D. Metzger 2022). The absolute maximum RM expected from this plasma is $|{\rm RM}|_{\rm max} \sim 10^7\,{\rm rad\,m^{-2}}$, which is consistent with the observed value of $\sim$4700 rad m^{-2} (see Equation (50) of N. Sridhar & B. D. Metzger 2022).

ORCID iDs

Alexandra M. Moroianu https://orcid.org/0000-0003-1936-9062
Shivani Bhandari https://orcid.org/0000-0003-3460-506X
Maria R. Drout https://orcid.org/0000-0001-7081-0082
Jason W. T. Hessels https://orcid.org/0000-0003-2317-1446
Danté M. Hewitt https://orcid.org/0000-0002-5794-2360
Franz Kirsten https://orcid.org/0000-0001-6664-8668
Benito Marcote https://orcid.org/0000-0001-9814-2354
Ziggy Pleunis https://orcid.org/0000-0002-4795-697X
Mark P. Snelders https://orcid.org/0000-0001-6170-2282
Navin Sridhar https://orcid.org/0000-0002-5519-9550
Uwe Bach https://orcid.org/0000-0002-7722-8412
Emmanuel K. Bempong-Manful https://orcid.org/0000-0002-1727-1224
Vladislavs Bezrukovs https://orcid.org/0000-0003-3655-2280
Richard Blaauw https://orcid.org/0000-0003-1771-1012
Justin D. Bray https://orcid.org/0000-0002-0963-0223
Salvatore Buttaccio https://orcid.org/0000-0002-3341-466X
Shami Chatterjee https://orcid.org/0000-0002-2878-1502
Alessandro Corongiu https://orcid.org/0000-0002-5924-3141
Roman Feiler https://orcid.org/0000-0002-9812-2078
B. M. Gaensler https://orcid.org/0000-0002-3382-9558
Marcin P. Gawroński https://orcid.org/0000-0003-4056-4903
Marcello Giroletti https://orcid.org/0000-0002-8657-8852
Adaeze L. Ibik https://orcid.org/0000-0003-2405-2967
Ramesh Karuppusamy https://orcid.org/0000-0002-5307-2919
Mattias Lazda https://orcid.org/0000-0002-5857-4264
Calvin Leung https://orcid.org/0000-0002-4209-7408
Michael Lindqvist https://orcid.org/0000-0002-3669-0715
Kiyoshi W. Masui https://orcid.org/0000-0002-4279-6946
Daniele Michilli https://orcid.org/0000-0002-2551-7554
Kenzie Nimmo https://orcid.org/0000-0003-0510-0740
Omar S. Ould-Boukattine https://orcid.org/0000-0001-9381-8466
Ayush Pandhi https://orcid.org/0000-0002-8897-1973
Zsolt Paragi https://orcid.org/0000-0002-5195-335X
Aaron B. Pearlman https://orcid.org/0000-0002-8912-0732
Weronika Puchalska https://orcid.org/0000-0003-2422-6605
Paul Scholz https://orcid.org/0000-0002-7374-7119
Kaitlyn Shin https://orcid.org/0000-0002-6823-2073
Matteo Trudu https://orcid.org/0000-0002-1530-0474

David Williams-Baldwin https://orcid.org/0000-0001-7361-0246
Jun Yang https://orcid.org/0000-0002-2322-5232

References

Agarwal, D., Aggarwal, K., Burke-Spolaor, S., Lorimer, D. R., & Garver-Daniels, N. 2020, MNRAS, 497, 1661
Aggarwal, K., Budavári, T., Deller, A. T., et al. 2021, ApJ, 911, 95
Aguilera-Dena, D. R., Langer, N., Moriya, T. J., & Schootemeijer, A. 2018, ApJ, 858, 115
Amiri, M., Andersen, B. C., Bandura, K., et al. 2021, ApJS, 257, 59
Anna-Thomas, R., Connor, L., Dai, S., et al. 2023, Sci, 380, 599
Astropy Collaboration, Robitaille, T. P., Tollerud, E. J., et al. 2013, A&A, 558, A33
Balaubramanian, A., Bhardwaj, M., & Tendulkar, S. P. 2025, ApJ, 995, 51
Baldwin, A., Phillips, M. M., & Terlevich, R. 1981, PASP, 93, 817
Bassa, C. G., Tendulkar, S. P., Adams, E. A. K., et al. 2017, ApJL, 843, L8
Beniamini, P., Kumar, P., & Narayan, R. 2022, MNRAS, 510, 4654
Bernales-Cortes, L., Tejos, N., Prochaska, J. X., et al. 2025, A&A, 696, A81
Bhandari, S., Heintz, K. E., Aggarwal, K., et al. 2022, AJ, 163, 69
Bhandari, S., Marcote, B., Sridhar, N., et al. 2023, ApJL, 958, L19
Bhardwaj, M., Balasubramanian, A., Kaushal, Y., & Tendulkar, S. P. 2025a, arXiv:2506.23861
Bhardwaj, M., Kirichenko, A. Y., Michilli, D., et al. 2021, ApJL, 919, L24
Bhardwaj, M., Snelders, M. P., Hessels, J. W. T., et al. 2025b, ApJL, 992, L35, arXiv:2506.11915
Bhattacharya, M., Murase, K., & Kashiyama, K. 2024, arXiv:2412.19358
Bhusare, Y., Maan, Y., & Kumar, A. 2025, ApJ, 993, 234
Bochenek, C. D., Ravi, V., Belov, K. V., et al. 2020, Natur, 587, 59
Brentjens, M. A., & de Bruyn, A. G. 2005, A&A, 441, 1217
Bruni, G., Piro, L., Yang, Y.-P., et al. 2024, Natur, 632, 1014
Bruni, G., Piro, L., Yang, Y. P., et al. 2025, A&A, 695, L12
Callingham, T. M., Cautun, M., Deason, A. J., et al. 2019, MNRAS, 484, 5453
Cardelli, J. A., Clayton, G. C., & Mathis, J. S. 1989, ApJ, 345, 245
CASA Team, Bean, B., Bhatnagar, S., et al. 2022, PASP, 134, 114501
Chatterjee, S., Law, C. J., Wharton, R. S., et al. 2017, Natur, 541, 58
Chen, X.-L., Tsai, C.-W., Li, D., et al. 2025, ApJL, 980, L24
CHIME/FRB Collaboration, Amiri, M., Amouyal, D., et al. 2025, ApJS, 280, 6
CHIME/FRB Collaboration, Amiri, M., Bandura, K., et al. 2018, ApJ, 863, 48
CHIME/FRB Collaboration, Andersen, B. C., Bandura, K., et al. 2023, ApJ, 947, 83
CHIME/FRB Collaboration, Andersen, B. C., Bandura, K. M., et al. 2020, Natur, 587, 54
Cook, A. M., Bhardwaj, M., Gaensler, B. M., et al. 2023, ApJ, 946, 58
Cordes, J. M., & Lazio, T. J. W. 2002, arXiv:astro-ph/0207156
Curtin, A. P., Sand, K. R., Pleunis, Z., et al. 2025, ApJ, 992, 206
Desvignes, G., Eatough, R. P., Pen, U. L., et al. 2018, ApJL, 852, L12
Dey, A., Schlegel, D. J., Lang, D., et al. 2019, AJ, 157, 168
Diemer, B. 2018, ApJS, 239, 35
Diemer, B., & Joyce, M. 2019, ApJ, 871, 168
Dong, Y., Eftekhari, T., Fong, W., et al. 2024a, ApJ, 973, 133
Dong, Y., Eftekhari, T., Fong, W.-f., et al. 2024b, ApJ, 961, 44
Drake, S. A., & Ulrich, R. K. 1980, BAAS, 12, 798
Eatough, R. P., Falcke, H., Karuppusamy, R., et al. 2013, Natur, 501, 391
Eftekhari, T., Berger, E., Margalit, B., Metzger, B. D., & Williams, P. K. G. 2020, ApJ, 895, 98
Feng, Y., Li, D., Yang, Y.-P., et al. 2022, Sci, 375, 1266
Feng, Y., Zhang, Y.-K., Xie, J., et al. 2025, SCPMA, 68, 289511
Flewelling, H. A., Magnier, E. A., Chambers, K. C., et al. 2020, ApJS, 251, 7
Fong, W.-f., Dong, Y., Leja, J., et al. 2021, ApJL, 919, L23
Fonseca, E., Andersen, B. C., Bhardwaj, M., et al. 2020, ApJL, 891, L6
Gaensler, B. M., & Slane, P. O. 2006, ARA&A, 44, 17
Giodini, S., Pierini, D., Finoguenov, A., et al. 2009, ApJ, 703, 982
Gordon, A. C., Fong, W.-f., Kilpatrick, C. D., et al. 2023, ApJ, 954, 80
Gordon, A. C., Fong, W.-f., Simha, S., et al. 2024, ApJL, 963, L34
Gould, D. M., & Lyne, A. G. 1998, MNRAS, 301, 235
Haverkorn, M. 2015, ASSL, 407, 483
Heger, A., Fryer, C. L., Woosley, S. E., Langer, N., & Hartmann, D. H. 2003, ApJ, 591, 288
Heintz, K. E., Prochaska, J. X., Simha, S., et al. 2020, ApJ, 903, 152
Hilmarsson, G. H., Spitler, L. G., Main, R. A., & Li, D. Z. 2021, MNRAS, 508, 5354
Hirschauer, A. S., Salzer, J. J., Janowiecki, S., & Wegner, G. A. 2018, AJ, 155, 82
Hogg, D. W. 1999, arXiv:astro-ph/9905116
Hook, I. M., Jørgensen, I., Allington-Smith, J. R., et al. 2004, PASP, 116, 425
Hu, C.-R., & Huang, Y.-F. 2023, ApJS, 269, 17
Ibik, A. L., Drout, M. R., Gaensler, B. M., et al. 2024, ApJ, 976, 2
Johnson, B. D., Leja, J., Conroy, C., & Speagle, J. S. 2021, ApJS, 254, 22
Keimpema, A., Kettenis, M. M., Pogrebenko, S. V., et al. 2015, ExA, 39, 259
Kewley, L. J., & Ellison, S. L. 2008, ApJ, 681, 1183
Khrykin, I. S., Ata, M., Lee, K.-G., et al. 2024, ApJ, 973, 151
Kirsten, F., Marcote, B., Nimmo, K., et al. 2022, Natur, 602, 585
Kirsten, F., Snelders, M. P., Jenkins, M., et al. 2021, NatAs, 5, 414
Kobulnicky, H. A., & Kewley, L. J. 2004, ApJ, 617, 240
Kravtsov, A. V. 2013, ApJL, 764, L31
Law, C. J., Sharma, K., Ravi, V., et al. 2024, ApJ, 967, 29
Lee, K.-G., Khrykin, I. S., Simha, S., et al. 2023, ApJL, 954, L7
Levesque, E. M., Kewley, L. J., Berger, E., & Zahid, H. J. 2010, AJ, 140, 1557
Levesque, E. M., Stringfellow, G. S., Ginsburg, A. G., Bally, J., & Keeney, B. A. 2014, AJ, 147, 23
Li, C. K., Lin, L., Xiong, S. L., et al. 2021, NatAs, 5, 378
Li, D., Wang, P., Zhu, W. W., et al. 2021, Natur, 598, 267
Lorimer, D. R., 2011 Astrophysics Source Code Library, ascl:1107.016
Lorimer, D. R., Bailes, M., McLaughlin, M. A., Narkevic, D. J., & Crawford, F. 2007, Sci, 318, 777
Lunnan, R., Chornock, R., Berger, E., et al. 2014, ApJ, 787, 138
Macquart, J. P., Prochaska, J. X., McQuinn, M., et al. 2020, Natur, 581, 391
Manchester, R. N., Hobbs, G. B., Teoh, A., & Hobbs, M. 2005, AJ, 129, 1993
Marcote, B., Paragi, Z., Hessels, J. W. T., et al. 2017, ApJL, 834, L8
Marcote, B., Nimmo, K., Hessels, J. W. T., et al. 2020, Natur, 577, 190
Margalit, B., & Metzger, B. D. 2018, ApJL, 868, L4
Margalit, B., Metzger, B. D., Berger, E., et al. 2018, MNRAS, 481, 2407
McClintock, T., Rozo, E., Becker, M. R., et al. 2019, ApJ, 872, 53
Mckinven, R., Gaensler, B. M., Michilli, D., et al. 2023, ApJ, 951, 82
McMullin, J. P., Waters, B., Schiebel, D., Young, W., & Golap, K. 2007, ASPC, 376, 127
Mereghetti, S., Savchenko, V., Ferrigno, C., et al. 2020, ApJL, 898, L29
Metzger, B. D., Berger, E., & Margalit, B. 2017, ApJ, 841, 14
Mezcua, M., Hlavacek-Larrondo, J., Lucey, J. R., et al. 2018, MNRAS, 474, 1342
Michilli, D., Bhardwaj, M., Brar, C., et al. 2023, ApJ, 950, 134
Michilli, D., Seymour, A., Hessels, J. W. T., et al. 2018, Natur, 553, 182
Muno, M. P., Clark, J. S., Crowther, P. A., et al. 2006, ApJL, 636, L41
Murase, K., Kashiyama, K., & Mészáros, P. 2016, MNRAS, 461, 1498
Murphy, E. J., Condon, J. J., Schinnerer, E., et al. 2011, ApJ, 737, 67
Navarro, J. F., Frenk, C. S., & White, S. D. M. 1996, ApJ, 462, 563
Ng, C., Pandhi, A., Mckinven, R., et al. 2025, ApJ, 982, 154
Nimmo, K., Hewitt, D. M., Hessels, J. W. T., et al. 2022, ApJL, 927, L3
Niu, C. H., Aggarwal, K., Li, D., et al. 2022, Natur, 606, 873
Ocker, S. K., Anderson, L. D., Lazio, T. J. W., Cordes, J. M., & Ravi, V. 2024, ApJ, 974, 10
Ocker, S. K., & Cordes, J. M. 2024, RNAAS, 8, 17
Osterbrock, D. E., & Ferland, G. J. 2006, Astrophysics of Gaseous Nebulae and Active Galactic Nuclei (Univ. Science Books)
Ould-Boukattine, O. S., Cooper, A. J., Hessels, J. W. T., et al. 2025, arXiv:2509.16374
Pandhi, A., Pleunis, Z., Mckinven, R., et al. 2024, ApJ, 968, 50
Petrov, L. Y., & Kovalev, Y. Y. 2025, ApJS, 276, 38
Pettini, M., & Pagel, B. E. J. 2004, MNRAS, 348, L59
Piro, A. L., & Gaensler, B. M. 2018, ApJ, 861, 150
Piro, L., Bruni, G., Troja, E., et al. 2021, A&A, 656, L15
Planck Collaboration, Aghanim, N., Akrami, Y., et al. 2020, A&A, 641, A6
Plavin, A., Paragi, Z., Marcote, B., et al. 2022, MNRAS, 511, 6033
Pleunis, Z., Good, D. C., Kaspi, V. M., et al. 2021, ApJ, 923, 1
Prayag, V., Levin, L., Geyer, M., et al. 2024, MNRAS, 533, 2570
Prestwich, A. H., Tsantaki, M., Zezas, A., et al. 2013, ApJ, 769, 92
Prochaska, J. X., & Zheng, Y. 2019, MNRAS, 485, 648
Purcell, C. R., Van Eck, C. L., West, J., Sun, X. H., & Gaensler, B. M., 2020 Astrophysics Source Code Library, ascl:2005.003
Rahaman, S. M., Acharya, S. K., Beniamini, P., & Granot, J. 2025, ApJ, 988, 276, arXiv:2504.01125
Ravi, V., Catha, M., Chen, G., et al. 2025, AJ, 169, 330
Ravi, V., Law, C. J., Li, D., et al. 2022, MNRAS, 513, 982
Raynaud, R., Guilet, J., Janka, H.-T., & Gastine, T. 2020, SciA, 6, eaay2732
Reines, A. E., Condon, J. J., Darling, J., & Greene, J. E. 2020, ApJ, 888, 36
Rhodes, L., Caleb, M., Stappers, B. W., et al. 2023, MNRAS, 525, 3626
Ridnaia, A., Svinkin, D., Frederiks, D., et al. 2021, NatAs, 5, 372

Schlafly, E. F., & Finkbeiner, D. P. 2011, ApJ, 737, 103
Schootemeijer, A., Lennon, D. J., Garcia, M., et al. 2022, A&A, 667, A100
Sharma, K., Ravi, V., Connor, L., et al. 2024, Natur, 635, 61
Shepherd, M. C. 1997, ASPC, 125, 77
Siegel, S., & Fonseca, E. 2025, in 246th Meeting of the American Astronomical Society, 246, 317.03
Simha, S., Lee, K.-G., Prochaska, J. X., et al. 2023, ApJ, 954, 71
Snelders, M. P., Hessels, J. W. T., Huang, J., et al. 2025, arXiv:2510.11352
Song, C.-Y., & Liu, T. 2023, ApJ, 952, 156
Sridhar, N., & Metzger, B. D. 2022, ApJ, 937, 5
Sridhar, N., Metzger, B. D., Beniamini, P., et al. 2021, ApJ, 917, 13
Sridhar, N., Metzger, B. D., & Fang, K. 2024, ApJ, 960, 74
Svensson, K. M., Levan, A. J., Tanvir, N. R., Fruchter, A. S., & Strolger, L. G. 2010, MNRAS, 405, 57
Sydnor, J., Burke-Spolaor, S., Aggarwal, K., et al. 2025, ApJ, 984, 178
Tavani, M., Casentini, C., Ursi, A., et al. 2021, NatAs, 5, 401
Tendulkar, S. P., Bassa, C. G., Cordes, J. M., et al. 2017, ApJL, 834, L7
Tendulkar, S. P., Gil de Paz, A., Kirichenko, A. Y., et al. 2021, ApJL, 908, L12
Theureau, G., Parent, D., Cognard, I., et al. 2011, A&A, 525, A94
Tian, J., Pastor-Marazuela, I., Stappers, B., et al. 2024, ATel, 16446, 1
Tinker, J., Kravtsov, A. V., Klypin, A., et al. 2008, ApJ, 688, 709
Tremonti, C. A., Heckman, T. M., Kauffmann, G., et al. 2004, ApJ, 613, 898
van Bemmel, I. M., Kettenis, M., Small, D., et al. 2022, PASP, 134, 114502
van Straten, W., & Bailes, M. 2011, PASA, 28, 1
Wang, P., Zhang, J. S., Yang, Y. P., et al. 2025, arXiv:2507.15790
Wen, Z. L., & Han, J. L. 2024, ApJS, 272, 39
Yamasaki, S., Hashimoto, T., Kusakabe, H., & Goto, T. 2025, arXiv:2508.07688
Yang, Y.-P., Li, Q.-C., & Zhang, B. 2020, ApJ, 895, 7
Zampieri, L., & Roberts, T. P. 2009, MNRAS, 400, 677
Zhang, J.-S., Wang, T.-C., Wang, P., et al. 2025, arXiv:2507.14707
Zhang, Y.-K., Wang, P., Feng, Y., et al. 2022, RAA, 22, 124002
Zhao, Z. Y., Chen, K., Wang, F. Y., & Dai, Z.-G. 2024, MNRAS, 530, 1644